# Molecular and cellular dynamics of the developing human neocortex at single-cell resolution

**Authors:** Li Wang[1,2]*#, Cheng Wang[1,2]*, Juan A. Moriano[3], Songcang Chen[1,2], Shaobo Zhang[4], Tanzila Mukhtar[1,2], Shaohui Wang[1,2], Arantxa Cebrián-Silla[1,5], Qiuli Bi[1,2], Jonathan J. Augustin[1,2], Lilian Gomes de Oliveira[1,6],  Mengyi Song[1,2], Xinxin Ge[7], Guolong Zuo[1,2], Mercedes F. Paredes[1,2], Eric J. Huang[1,8], Arturo Alvarez-Buylla[1,5], Xin Duan[4,7], Jingjing Li[1,2]#, Arnold R. Kriegstein[1,2]#

[1]The Eli and Edythe Broad Center of Regeneration Medicine and Stem Cell Research, University of California San Francisco; San Francisco, CA 94143, USA.

[2]Department of Neurology, University of California San Francisco; San Francisco, CA 94143, USA.

[3]University of Barcelona Institute of Complex Systems; Barcelona, 08007, Spain

[4]Department of Ophthalmology, University of California San Francisco; San Francisco, CA 94143, USA.

[5]Department of Neurological Surgery, University of California San Francisco; San Francisco, CA 94143, USA.

[6]Neuro-immune Interactions Laboratory, Institute of Biomedical Sciences, Department of Immunology, University of São Paulo; São Paulo, SP 05508-220, Brazil

[7]Department of Physiology, University of California San Francisco, San Francisco, CA 94143, USA.

[8]Department of Pathology, University of California San Francisco; San Francisco, CA 94143, USA.

*These authors contributed equally to this work.

#Corresponding author. e-mail: Li.Wang@ucsf.edu; Jingjing.Li@ucsf.edu; Arnold.Kriegstein@ucsf.edu.

## Summary

The development of the human neocortex is a highly dynamic process and involves complex cellular trajectories controlled by cell-type-specific gene regulation[1]. Here, we collected paired single-nucleus chromatin accessibility and transcriptome data from 38 human neocortical samples encompassing both the prefrontal cortex and primary visual cortex. These samples span five main developmental stages, ranging from the first trimester to adolescence. In parallel, we performed spatial transcriptomic analysis on a subset of the samples to illustrate spatial organization and intercellular communication. This atlas enables us to catalog cell type-, age-, and area-specific gene regulatory networks underlying neural differentiation. Moreover, combining single-cell profiling, progenitor purification, and lineage-tracing experiments, we have untangled the complex lineage relationships among progenitor subtypes during the

40  transition from neurogenesis to gliogenesis in the human neocortex. Specifically, we find a
41  tripotential intermediate progenitor subtype termed Tri-IPC responsible for the local production
42  of GABAergic neurons. Furthermore, by integrating our atlas data with large-scale GWAS data,
43  we created a disease-risk map highlighting enriched ASD risk in second-trimester
44  intratelencephalic projection neurons. Our study sheds light on the gene regulatory landscape and
45  cellular dynamics of the developing human neocortex.

46

47  **Main Text**

48  Human neocortex development is a complex and coordinated process crucial for establishing the
49  brain's intricate structure and functionality. In the developing neocortex, radial glia (RGs)
50  generate glutamatergic excitatory neurons (ENs) in a characteristic inside-out pattern, with deep-
51  layer neurons produced first, followed by upper-layer intratelencephalic (IT) projection neurons[1].
52  Subsequently, ENs migrate along the radial glial scaffold to the cortical plate, where they
53  differentiate and form distinct cortical layers with coordinated synaptic connections. Meanwhile,
54  GABAergic inhibitory neurons (INs) originating in the ganglionic eminence migrate to the
55  cortex through the marginal and germinal zones, eventually becoming cortical interneurons of
56  the adult cortex. During the late second trimester, RGs transition from neurogenesis to
57  gliogenesis, producing astrocytes and oligodendrocyte lineage cells that populate the cortex.
58  Cell-type-specific gene regulatory mechanisms that underlie cell proliferation and differentiation
59  govern these highly regulated processes. However, our understanding of these mechanisms
60  remains incomplete.

61  Gene regulation involves epigenetic reprogramming and subsequent gene expression changes[2].
62  Over the past decade, single-cell transcriptome[3–13] and chromatin accessibility[14–16] analyses have
63  expanded our knowledge of cellular diversity and the molecular changes that occur during
64  human neocortical development. However, in many instances, measurements of the
65  transcriptome and epigenome were conducted independently, limiting our understanding of how
66  these two modalities coordinate with each other to form regulatory networks in the same cell. A
67  recent study explored gene-regulatory mechanisms in the developing human cortex by profiling
68  chromatin accessibility and gene expression within the same nuclei[17]. However, the analysis was
69  confined to a restricted number of samples and cell types, warranting further exploration to
70  obtain a more comprehensive understanding.

71  In this study, we conducted paired RNA sequencing (RNA-seq) and assay for transposase-
72  accessible chromatin with sequencing (ATAC-seq) on single nuclei derived from multiple
73  regions and age groups of the developing human neocortex. In addition, spatial transcriptomic
74  analysis was utilized to reveal cellular niches and cell-cell communication. These datasets have
75  enabled the construction of a multi-omic atlas of the human neocortex across different
76  developmental stages at single-cell resolution. Leveraging this atlas, we delve into understanding
77  molecular and cellular dynamics of the developing human neocortex, including cellular
78  composition, spatial organization, intercellular signaling, gene regulatory networks, lineage
79  potential, and disease susceptibility. Our results highlight novel multipotential intermediate
80  progenitor cells (IPCs) and cellular trajectories and shed light on the mechanisms of
81  neuropsychiatric disorders.

82  **Results**

2

*A single-cell multi-omic survey of the developing human neocortex*

To characterize transcriptomic and epigenomic changes during human neocortex development, we obtained 27 brain specimens and 38 unique biological samples across five major developmental stages ranging from the first trimester to adolescence, covering key events such as neurogenesis, neuronal migration, gliogenesis, synaptogenesis, and myelination (Fig. 1a, Supplementary Table 1). In addition, we included samples from both the prefrontal cortex (PFC) and primary visual cortex (V1), two poles of the rostral-caudal axis of the neocortex, to understand regional diversity. Applying the single-nucleus multiome (snMultiome) technique from 10X Genomics, we obtained paired single-nucleus ATAC-seq and RNA-seq data from 243,535 nuclei after quality control (see Methods). Some early-stage samples included brain regions other than the neocortex, such as the diencephalon and striatum (Extended Data Fig. 1a–d). We removed non-neocortical nuclei to focus our analysis on the neocortex, resulting in 232,328 nuclei in the final dataset (Supplementary Table 2). We detected similar numbers of genes, transcripts, and ATAC peak region fragments across different samples, with a median of 2289 genes, 4840 transcripts, and 4121 ATAC peak region fragments per nucleus (Extended Data Fig. 2a).

We performed weighted nearest neighbor analysis[18] to integrate information from the paired ATAC and RNA modalities. The resulting nearest neighbor graph was used for uniform manifold approximation and projection (UMAP) embedding and clustering. We used previously established hierarchical cortical cell-type architecture in the developing and adult human neocortex[11,19] as references for cluster annotation. Meanwhile, we took into consideration that cell identities can be ambiguous and transient during development. Therefore, we carefully evaluated the expression of marker genes (Extended Data Fig. 3, Supplementary Table 3) and determined 5 classes, 11 subclasses, and 33 high-fidelity cell types (Fig. 1b, Extended Data Fig. 2b, Supplementary Table 2). As expected, cells primarily clustered according to their lineages and, within individual lineages, further clustered by types, age groups, and regions (Fig. 1b,c). ENs, oligodendrocytes, and astrocytes showed strong regional differences (Fig. 1b,c). By contrast, INs, oligodendrocyte precursor cells (OPCs), microglia, and vascular cells lacked strong region specificity (Fig. 1b,c). Compared with UMAP embeddings based on either ATAC or RNA, embeddings based on both modalities had a more precise separation between cell types, age groups, and regions, suggesting that combination of both modalities better delineates spatiotemporal cell identities (Extended Data Fig. 2c).

Cell type proportions were comparable between samples of the same age group and region (Extended Data Fig. 2a). However, cell type proportions became substantially different when samples across age groups or regions were compared (Fig. 1d, Supplementary Table 3). Specifically, progenitors (e.g., RG-vRGs [moderated t-test, $P_{adj.}$ = 1.61E−06] and IPC-ENs [$P_{adj.}$ = 9.03E−06]) and immature neurons (e.g., EN-Newborns [$P_{adj.}$ = 9.42E−08] and EN-IT-Immatures [$P_{adj.}$ = 2.48E−09]) were more abundant in the first and second trimester but became depleted at later stages. Conversely, proportions of upper-layer intratelencephalic (IT) neurons (e.g., EN-L2_3-ITs [$P_{adj.}$ = 1.17E−03] and EN-L4-ITs [$P_{adj.}$ = 1.14E−03]) and macroglia (e.g., Astrocyte- Protoplasmic [$P_{adj.}$ = 6.27E−06] and Oligodendrocytes [$P_{adj.}$ = 3.14E−11]) became more abundant after birth. Moreover, EN-L4-ITs were more abundant in V1 than in PFC after the third trimester ($P_{adj.}$ = 1.10E−02), consistent with the expansion of the thalamorecipient layer 4 in V1.
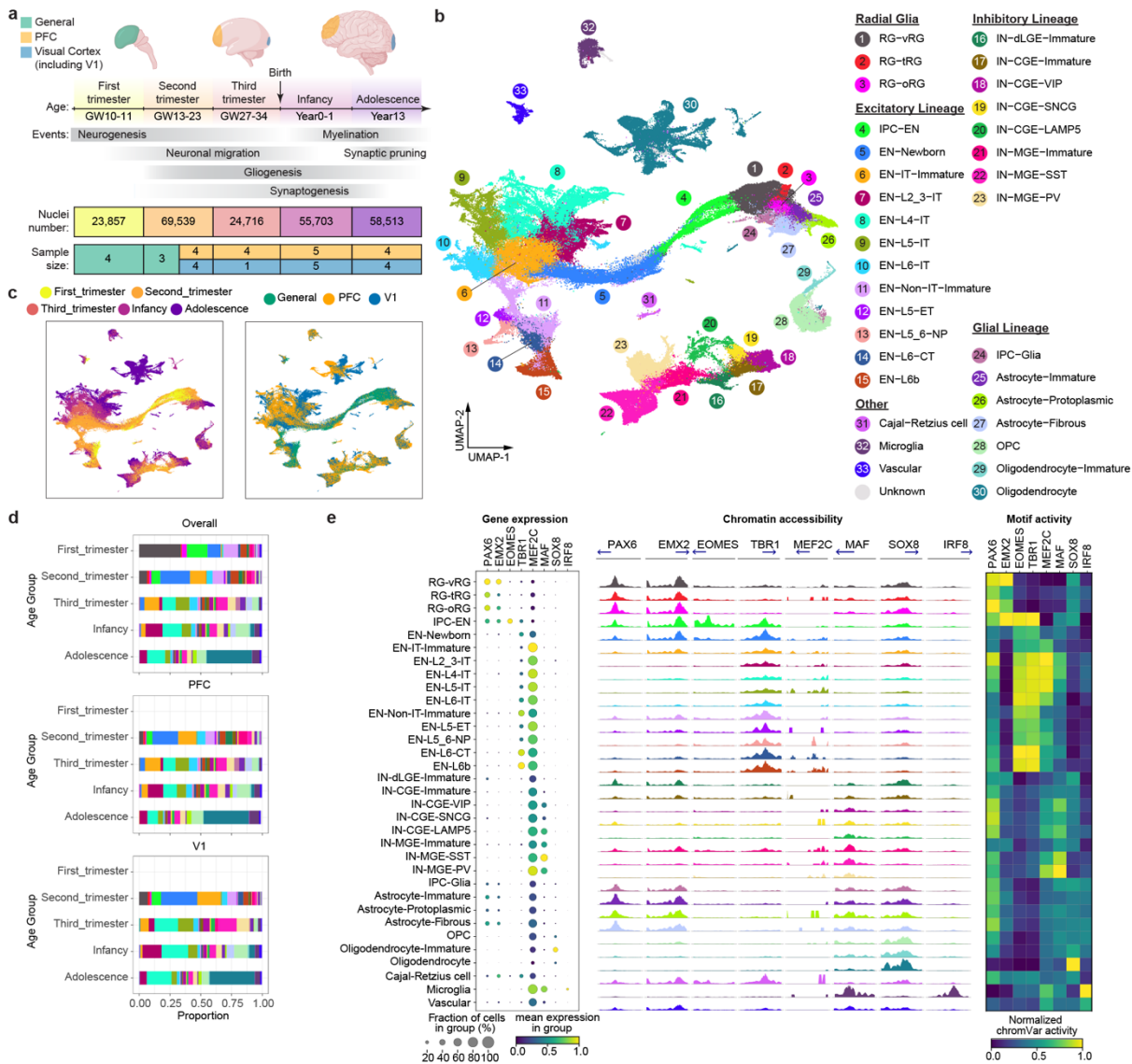
3

**Fig. 1 | A multi-omic survey of the developing human neocortex. a**, Description of samples used in this study. **b**, UMAP plots of the snMultiome data showing the distribution of 33 cell types. **c**, UMAP plots showing the distribution of age groups (left) and regions (right). **d**, Proportion of individual cell types across developmental stages and cortical regions. Bars are color-coded by cell types, the legend of which can be found in panel a. **e**, Left, dotplot of the signature transcriptional factors (TFs) in individual cell types. Middle, aggregated chromatin accessibility profiles on the promoter of signature TFs across cell types. The blue arrow represents each TF's transcriptional starting site and gene body. Right, heatmap of normalized chromVar motif activity of signature TFs across cell types.

127    To further evaluate data quality, we compared gene expression, chromatin accessibility, and
128    transcriptional regulatory activities of lineage-specific transcription factors (TFs) across cell
129    types (Supplementary Table 4). We found that the three attributes were concordant with each
130    other at most genomic loci (Fig. 1e). For example, *PAX6* and *EMX2*, two TFs critical for cortical
131    neural progenitor specification[20], were selectively expressed, had high promoter accessibility,
132    and exhibited enriched motif activities in RGs (Fig. 1e). Similar results were obtained with other
133    lineage-specific TFs. Thus, dynamic changes in epigenome and transcriptome are highly
134    coordinated during human neocortex development.

4

*Molecularly defined cytoarchitecture of the developing human neocortex*

To localize the observed cell types from our snMultiome data, we performed spatial transcriptomic analysis of the developing human neocortex using multiplexed error-robust fluorescence in situ hybridization (MERFISH)[21]. First, guided by the snMultiome data, we designed a 300-gene panel composed of gene markers for the main cell types in the developing cortex (Fig. 1b, Supplementary Table 5). We then analyzed their expression patterns in PFC and V1 at three age groups from the second trimester to infancy (Supplementary Table 5). From six samples, we retained 404,030 high-quality cells, resulting in 29 cell types that had one-to-one correspondence to those at similar stages in the snMultiome data (Fig. 2a, Extended Data Fig. 4a,b, Supplementary Table 6). To determine the cytoarchitecture of the developing neocortex, we defined a cell's neighborhood as each cell's 50 closest neighbors. We then unbiasedly divided cells into 10 niches based on the cell type composition of their neighborhoods. The 10 identified niches coincided well with histologically established cortical domains and were thus named after their closest counterpart (Fig. 2a).

Different cell types exhibited distinct patterns of niche distribution. Neural progenitors were primarily localized in the ventricular/subventricular zone (VZ/SVZ), whereas mature ENs were confined to their specific cortical layers throughout development (Fig. 2b, Extended Data Fig. 5a–f). Immature interneurons in the second trimester were enriched in both the marginal zone and VZ/SVZ, two routes they use to migrate into the cortex[22]. In the second trimester, the overall ratio of migrating interneurons in the marginal zone to VZ/SVZ was 1:4.1. Interestingly, this ratio was 1:3.3 for caudal ganglionic eminence (CGE)-derived interneurons and 1:5.2 for medial ganglionic eminence (MGE)-derived interneurons ($P < 2.2E−16$, Fisher's exact test), demonstrating lineage-specific preference in migration routes. This bias may contribute to the laminar distribution of interneuron subtypes at later stages, with CGE-derived interneurons enriched in upper layers and IN-MGE-PVs enriched in layers 4–6 (Fig. 2a,b, Extended Data Fig. 5a–f). The dorsal lateral ganglionic eminence (dLGE) primarily gives rise to olfactory bulb interneurons[23]. Interestingly, we observed immature INs expressing *MEIS2*, *SP8*, *TSHZ1*, and *PBX3*, presumably originating from dLGE (IN-dLGE-Immatures), in the white matter across all three age groups (Extended Data Fig. 5a–f). These neurons will likely constitute a subset of the white matter interstitial GABAergic interneurons in adulthood. Regarding glial cells, OPCs were evenly distributed between gray and white matter from the second trimester to infancy. However, oligodendrocytes were predominantly present in the white matter for all three age groups (Fig. 2b, Extended Data Fig. 5a–f). This difference supports a non-progenitor role of OPCs in cortical gray matter[24]. Microglia were highly enriched in the white matter (Fig. 2b, Extended Data Fig. 5a–f), consistent with their spatial distribution in the adult brain[25].

In early neonatal and adult mammalian brains, neurogenesis continues in the VZ/SVZ of the lateral ventricles, and the interneurons produced migrate to the olfactory bulb[26]. Most of these olfactory bulb interneurons are GABAergic but some could be glutamatergic[27]. We examined our perinatal PFC sample, which contained VZ/SVZ. We found a surprisingly large number of glutamatergic EN-Newborns, along with a small number of IPC-ENs, specifically within the SVZ (Extended Data Fig. 5c). Remarkably, within the VZ/SVZ of this sample, the count of EN-Newborns was 10.3-fold higher than that of IN-dLGE-Immatures, which are considered putative newborn GABAergic olfactory bulb interneurons. Whether these late-born EN-Newborns will migrate to the cortical gray matter, the subcortical white matter, or the olfactory bulb remains to be determined.
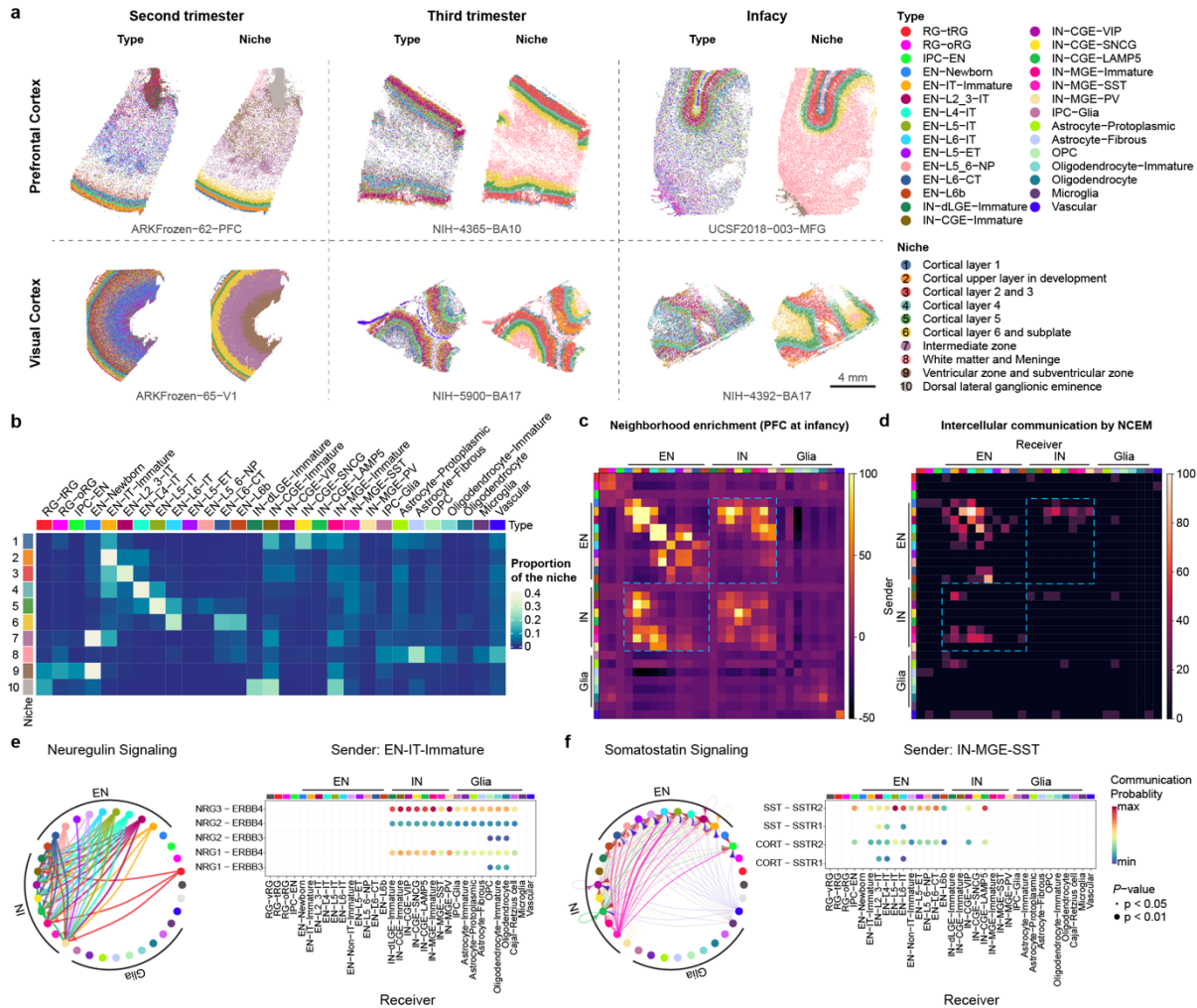
**Fig. 2 | Cell-cell communication in the developing human neocortex. a,** Spatial transcriptomic analysis of six neocortical samples. Cells are color-coded by types or the niches to which they belong. **b,** Proportion of different cell types in individual niches. Niche numbers correspond to the legend in panel a. **c,** Heatmap showing neighborhood enrichment scores of the PFC sample at infancy. The row and column annotations are color-coded by cell types, the legend of which can be found in panel a. **d,** Heatmap showing the percentage of significant intercellular communication determined by NCEM identified across all datasets. The row and column annotations are color-coded by cell types, the legend of which can be found in panel a. **e,** Left, Circular plot showing the direction of cellular interactions mediated by neuregulin signaling. Right, dotplot showing communication probability of example ligand-receptor pairs in the neuregulin signaling pathway from EN-IT-Immature to other cell types. Empty space means the communication probability is zero. P-values were calculated by one-sided permutation test. **f,** Left, Circular plot showing the direction of cellular interactions mediated by somatostatin signaling. Right, dotplot showing communication probability of example ligand-receptor pairs in the somatostatin signaling pathway from IN-MGE-SST to other cell types. Empty space means the communication probability is zero. P-values were calculated by one-sided permutation test.

## *Cell-cell communication in the developing human neocortex*

To identify cell-cell communication in the developing human neocortex, we first evaluated the spatial proximity of cell types in each MERFISH sample through neighborhood enrichment analysis. We found that different types of ENs were enriched in their own neighborhoods, consistent with their strong layer specificity. Interestingly, we also observed robust neighborhood enrichment between specific types of ENs and INs, such as EN-IT-Immatures and IN-CGE-VIPs,

186 as well as EN-L4-ITs and IN-MGE-SSTs (Fig. 2c, Extended Data Fig. 6a). To determine if the
187 gene expression of a cell type was influenced by its proximity to a neighboring cell type, we
188 performed node-centric expression modeling (NCEM)[28]. Cell communication inference via
189 NCEM revealed strong interactions among various types of ENs and between ENs and INs
190 across multiple datasets (Fig. 2d, Extended Data Fig. 6b, Supplementary Table 7). Notably, the
191 presence of EN-IT-Immatures (sender) affected gene expression in various IN types (receivers).
192 In contrast, the presence of IN-MGE-SSTs (sender) influenced gene expression in multiple EN
193 types (receivers).

194 Since most of the MERFISH samples were collected from stages preceding the peak of
195 synaptogenesis in humans, we resorted to ligand-receptor analysis using CellChat[29] to identify
196 potential mechanisms underlying the communication between ENs and INs (Extended Data Fig.
197 6c). Focusing on EN-IT-Immatures and IN-MGE-SSTs as ligand producing cells, we found that
198 neuregulin and somatostatin were potential mediators for their communication with INs and
199 ENs, respectively (Fig. 2e, Supplementary Table 8). Together, our findings highlight the
200 reciprocal communications between the two major neuronal subclasses during human cortical
201 development.

### *Gene regulatory networks in the developing human neocortex*

203 To establish the gene regulatory networks (GRNs) governing human neocortical development,
204 we employed SCENIC+[30], a computational framework that combines single-cell ATAC and gene
205 expression data with motif discovery to infer enhancer-driven regulons (eRegulons), linking
206 individual TFs to their respective candidate enhancers and target genes. Our analysis identified a
207 total of 582 eRegulons, comprising 385 transcriptional activators and 197 repressors
208 (Supplementary Table 9). These eRegulons collectively targeted 8134 regions and 8048 genes.
209 We quantified the activity of each eRegulon in each nucleus using the AUCell algorithm[31],
210 assessing region-based and gene-based AUC scores according to the overall accessibility of
211 target regions and expression levels of target genes, respectively.

212 Consistent with expectations, expression levels of transcriptional activators exhibited a positive
213 correlation with the AUC scores of their target regions and genes, whereas transcriptional
214 repressors negatively correlated with their targets (Extended Data Fig. 7a). Focusing on
215 activators, we not only recovered established master regulators of cortical progenitors (e.g.,
216 *EMX1* and *SALL1*), ENs (e.g., *FOXP1* and *TBR1*), INs (e.g., *ARX* and *LHX6*) but also uncovered
217 novel cell-type-specific eRegulons that potentially serve as lineage-determining factors (Fig. 3a,
218 Supplementary Table 10).

219 In addition, we observed that many cell-type-specific eRegulons shared target regions and target
220 genes (Extended Data Fig 7b). Notable instances included *TCF7L1* and *TCF7L2* in RG-vRGs,
221 *GLIS1* and *SMAD3* in EN-L4-ITs, *MAF* and *PRDM1* in IN-MGE-PVs, *PAX6* and *SOX9* in
222 Astrocyte-Protoplasmics, as well as *OLIG2* and *VSX1* in OPCs (Fig. 3b, Extended Data Fig. 7c–
223 d). This cooperative sharing of regulatory targets likely serves to increase the robustness of
224 GRNs against transcriptional noise or perturbations during cortical development.

### *Genetic programs that determine excitatory neuron identities*

226 Having established the GRNs, we sought to understand how the activation of cell-type-specific
227 eRegulons controls cortical neuron differentiation. To this end, we selected nuclei from EN
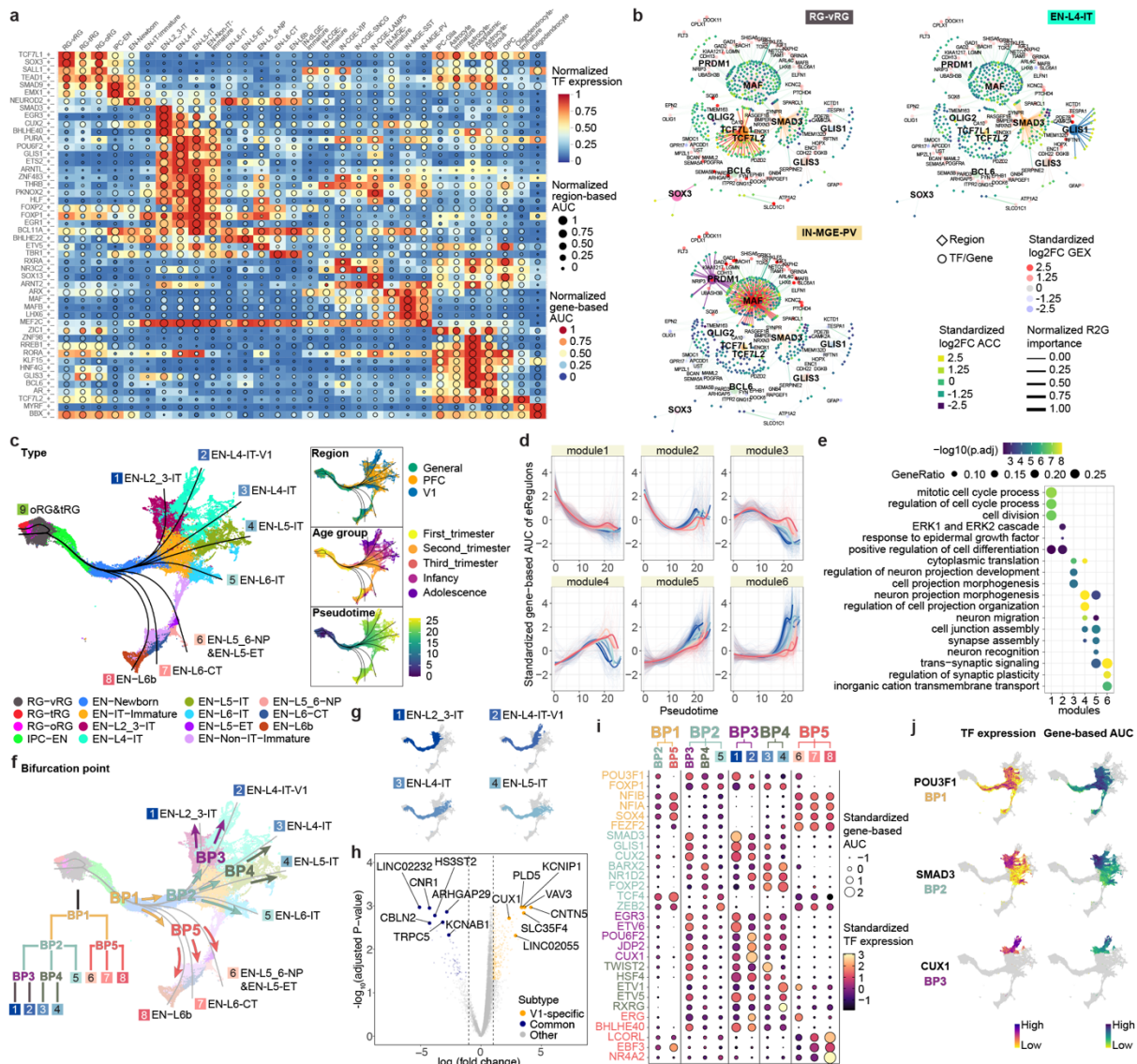228 lineages, inferred nine differentiation trajectories originating from RG-vRG, and calculated

7

**Fig. 3 | Gene regulatory networks that establish cell identities. a**, Heatmap-dotplot showing the min-max normalized TF expression levels, region-based AUC scores, and gene-based AUC scores of selective eRegulons across cell types. **b**, Gene regulatory networks of selective eRegulons in three distinct cell types (RG-vRG, EN-L4-IT, and IN-MGE-PV). TF nodes and their links to enhancers are individually colored. The size and the transparency of the TF nodes represent their gene expression levels in each cell type. **c**, UMAP plots of cells belonging to excitatory neuron lineages showing the nine trajectories. Cells are color-coded by types, regions, age groups, or pseudotime. **d**, Standardized gene-based AUC scores of six eRegulon modules along the trajectories of excitatory neuron lineages. eRegulons are color-coded by neuronal subtypes. Thick, non-transparent lines represent the average AUC scores of each module in each lineage. **e**, Gene ontology enrichment analysis for target genes of individual eRegulon modules. Empty space means adjusted P values > 0.05. Hypergeometric test; nominal P values were adjusted by the Benjamini and Hochberg method. **f**, Bifurcation points during excitatory neuron differentiation. **g**, Trajectories of four intratelencephalic neuron lineages. **h**, Volcano plots highlighting differentially expressed genes between V1-specific and common EN-L4-IT neurons. Likelihood ratio test; nominal P values were adjusted by the Benjamini and Hochberg method. **i**, Dotplot highlighting representative eRegulons (activators) involved in trajectory determination at bifurcation points. **j**, UMAP plots highlighting representative eRegulons involved in trajectory determination at bifurcation points.

pseudotime values for each nucleus (Fig. 3c, Extended Data Fig. 8a–f, Supplementary Table 11)[32]. Except for one trajectory leading to late-stage radial glia (oRG and tRG), the remaining

8

231  eight trajectories ended with terminally differentiated ENs. Utilizing a generalized additive
232  model[33], we analyzed eRegulon activity along each trajectory, categorizing all eRegulons into six
233  modules based on their temporal patterns of activity (Fig. 3d, Supplementary Table 12). Overall,
234  all six modules exhibited distinct activity patterns along the pseudotime but comparable patterns
235  across trajectories (Fig. 3d). Modules specifically active in the early, intermediate, and late stages
236  respectively promoted cell division, cell projection morphogenesis, and synaptic plasticity (Fig.
237  3e, Supplementary Table 12). These findings highlight that most eRegulons demonstrate
238  conserved activity across various types of ENs, governing shared cellular processes during
239  neuronal differentiation.

240  Our subsequent objective was to explore gene regulatory mechanisms that determine EN
241  identities. To achieve this, we pinpointed five bifurcation points (BPs) along the eight
242  differentiation trajectories (Fig. 3f). An intriguing finding emerged regarding EN-L4-ITs, which
243  delineated into two distinct trajectories based on their region of origin (Fig. 3c,f). Specifically,
244  the divergence occurred at BP2, where V1-specific EN-L4-ITs continued their trajectory
245  alongside EN-L2_3-IT, while the EN-L4-ITs shared between PFC and V1 followed a trajectory
246  partially overlapping with EN-L5-IT (Fig. 3f,g). To further discriminate between the two EN-L4-
247  IT subtypes, we performed differential gene expression analysis, identifying 1,908 differentially
248  expressed genes between V1-specific and common EN-L4-ITs (Fig. 3h, Extended Data Fig. 9a,b,
249  Supplementary Table 13). We then examined the expression patterns of top differentially
250  expressed genes using in situ hybridization (ISH) data from Allen Brain Atlas. Notably, *CUX1*
251  and *KCNIP1*, two genes preferentially expressed in V1-specific EN-L4-IT, exhibited stronger
252  ISH signals in layer 4 of V1 compared to the adjacent secondary visual cortex (V2) (Extended
253  Data Fig. 9c). In contrast, the common EN-L4-IT biased gene *KCNAB1* showed robust and
254  specific signals in layer 4 of V2 but only displayed scattered signals in V1 (Extended Data Fig.
255  9c). Moreover, both V1-specific and common EN-L4-ITs expressed markers of their counterparts
256  recently reported in the adult human cortex[34] (Extended Data Fig. 9d). These findings confirm
257  the presence of V1-specific EN-L4-ITs in the developing neocortex and underscore their distinct
258  developmental trajectory compared to EN-L4-ITs found in other cortical regions.

259  To identify eRegulons associated with lineage bifurcation, we segmented the differentiation
260  trajectories into five parts and conducted trajectory-based differential eRegulon activity analysis
261  within specific segments encompassing each BP (Extended Data Fig. 8g, Methods). Among the
262  top-ranked differentially active eRegulons at BPs were those featuring well-established TFs
263  crucial for cell identity acquisition, including *CUX2* for upper-layer IT neurons, *FEZF2* for non-
264  IT neurons, and *NR4A2* for EN-L6bs (Fig. 3i, Supplementary Table 14). Furthermore, our
265  analysis revealed novel candidate regulators at multiple levels of lineage bifurcation, such as
266  *POU3F1* for IT neurons, *SMAD3* for upper-layer IT neurons, and *CUX1* for V1-specific EN-L4-
267  ITs, among many others (Fig. 3i,j, Extended Data Fig. 8h). Collectively, these results reveal
268  genetic programs that control the divergence of EN identities.

269  ***Lineage potential of glial progenitors in the late second trimester***

270  Between gestational week 18 and 26, RGs in the human neocortex gradually transition from
271  neurogenesis to gliogenesis[35]. However, our understanding of gliogenesis in the human
272  neocortex is still limited compared to neurogenesis. In the snMultiome dataset, we identified a
273  total of 10 different cell types within the macroglia lineage, including three RGs types, IPC-Glia,
274  and other cell types associated with either the astrocyte or oligodendrocyte lineages (Extended
275  Data Fig. 10a,b). Among these cell types, *EGFR*high*OLIG2*+ IPC-Glia have been previously

276   reported by us and others as "pre-OPC"[36], "pri-OPC"[37], "mGPC"[15], "bMIPC"[38], or "GPC"[39] in
277   humans. A similar cell type has been noted in mice as "pri-OPC"[40], "tri-IPC"[41], or "MIPC"[42].
278   Studies using human tissue have demonstrated IPC-Glia's capacity to generate OPCs [36] and
279   astrocytes[39]. Moreover, genetic labeling experiments in mice suggested their additional potential
280   to produce olfactory bulb interneurons[41]. Despite these advancements, ongoing debates and
281   uncertainties persist regarding the origin and lineage potential of human glial progenitors,
282   especially in the late second trimester, when a variety of glial progenitor types emerge.

283   To address this uncertainty, we leveraged our snMultiome data collected between gestational
284   week 20 to 24 and explored the expression patterns of surface protein markers (Extended Data
285   Fig. 10c.d). We identified five proteins whose combinatorial expression effectively distinguishes
286   between different glial cell types in the late second trimester (Fig. 4a, Extended Data Fig. 10e).
287   Employing tissue dissection, surface protein staining, and fluorescence-activated cell sorting, we
288   isolated four different glial progenitors–RG-tRGs, RG-oRGs, IPC-Glia, and OPCs (Fig. 4b,
289   Extended Data Fig. 10f) from the late second-trimester human cortex. We first assessed the
290   isolated cells morphologically after culturing for five days in basal culture medium without
291   growth factor supplement (Fig. 4b). RG-tRGs and RG-oRGs were mostly unipolar, featuring a
292   large soma and a thick, long primary process akin to the radial fiber. IPC-Glia appeared mostly
293   bipolar or oligopolar, with shorter processes compared to RGs. OPCs exhibited a "bushy"
294   morphology, suggesting they had started differentiating into pre-myelinating oligodendrocytes.
295   Most cells in the OPC culture died within 8 days, consistent with their dependence on specific
296   growth factors for survival[39]. Thus, our subsequent analysis focused on the remaining three
297   progenitor types. We immunostained the sorted cells on day one in vitro (DIV1) to validate their
298   identities (Extended Data Fig. 11a–f). Isolated RG-tRGs and RG-oRGs were positive for the
299   progenitor marker, TFAP2C, whereas the tRG marker, CRYAB, was specifically expressed in
300   RG-tRGs. In contrast, IPC-Glia were positive for both OLIG2 and EGFR. Few cells across all
301   three cultures displayed positivity for the EN marker, NeuN, the astrocyte marker, SPARCL1, or
302   the IN lineage marker, DLX5. In addition, few cells were OLIG2$^+$ only, suggesting minimum
303   contamination from OPCs or oligodendrocytes.

304   Having validated our isolation strategy, we allowed cells to spontaneously differentiate without
305   growth factor supplement for 14 days and performed single-cell RNA-sequencing (scRNA-seq)
306   at DIV0, 7, and 14 to track their differentiation (Extended Data Fig. 11g–j). The scRNA-seq data
307   revealed a total of ten distinct cell types (Extended Data Fig. 11j,k, Methods). In the UMAP
308   space, cells clustered according to the stage of differentiation, the seeding cell type, and their
309   identity (Extended Data Fig. 11h–j). Data from DIV0 reaffirmed the identities of the sorted cells
310   (Fig. 4c, Extended Data Fig. 11l). On DIV7, three different types of descendants emerged in the
311   IPC-Glia culture—astrocytes (9.4%), OPCs (1.1%), and a notable population of IN lineage cells,
312   namely *DLX5$^+$BEST3$^+$* IPC-INs (26.2%) and *DLX5$^+$BEST3$^-$* INs (19.9%) (Fig. 4c, Extended
313   Data Fig. 11l). We hence renamed IPC-Glia as Tri-IPC to highlight their tripotency. The
314   relatively low proportion of OPCs observed (1.1% on DIV7 and 1.8% on DIV14) could be
315   attributed to the absence of specific growth factors required for their survival. In contrast, both
316   RG-tRGs and RG-oRGs differentiated into IPC-ENs at DIV7 and further into ENs by DIV14,
317   indicating their continued production of ENs into the late second trimester (Fig. 4c, Extended
318   Data Fig. 11l). Interestingly, Tri-IPCs emerged in both the RG-tRG and RG-oRG cultures by
319   DIV7 (3.0% and 6.3%), along with a small proportion of IPC-INs (1.0% and 3.0%) but not INs
320   (0.1% and 0.2%). By DIV14, astrocytes (0.7% and 1.8%), OPCs (1.5% and 1.8%), and INs
321   (5.4% and 9.1%) were all present (Fig. 4c, Extended Data Fig. 11l). The delayed appearance of
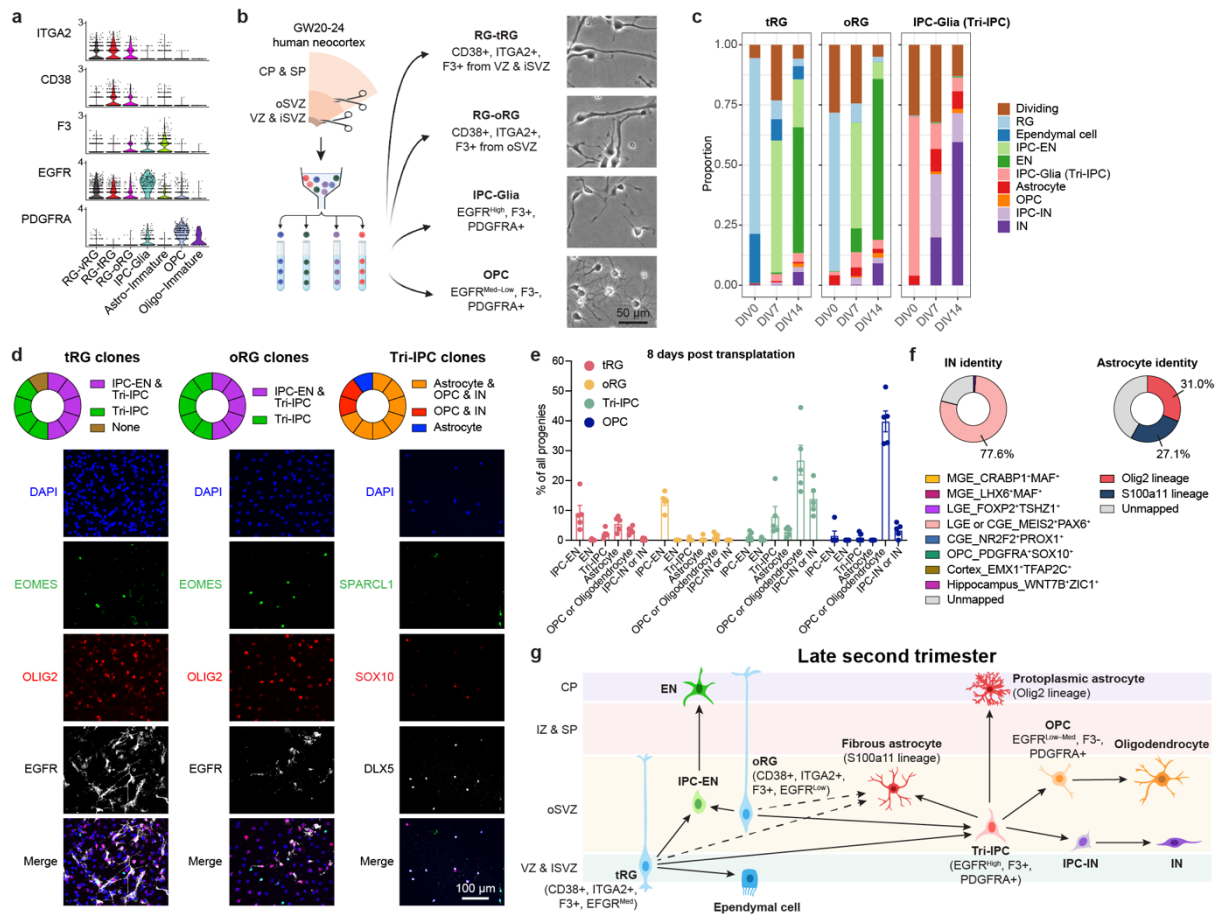
**Fig. 4 | Multipotent progenitors during transition from neurogenesis to gliogenesis. a**, Violin plots showing the expression patterns of surface proteins used for progenitor isolation. **b**, Left, schematic diagram showing the sorting strategy for isolation of progenitor subtypes. Right, phase-contrast images of progenitor subtypes after five days in culture. VZ & iSVZ, ventricular zone and inner subventricular zone; oSVZ, outer subventricular zone; CP & SP, cortical plate and subplate. **c**, Proportion of individual cell types across progenitor subtypes and differentiation stages. **d**, Clonal analysis demonstrating multipotency of individual progenitor cells (n = 10, 10, 10 clones). **e**, Quantification of progeny types after progenitor transplantation to acute cortical slices (n = 5, 5, 5, 5 samples), including IPC-EN (EOMES$^+$), EN (NeuN$^+$), Tri-IPC (OLIG2$^+$EGFR$^+$), astrocyte (SPARCL1+), OPC or oligodendrocyte (OLIG2$^+$EGFR$^-$), and IPC-IN or IN (DLX5$^+$). **f**, Prediction of identities of interneurons (INs) and astrocytes derived from Tri-IPCs. **g**, Graphical summary of cell lineage relationships in late second-trimester human neocortex.

INs from RG cultures was consistent with our recent report that oRGs can produce INs[43], but provided additional evidence that they do so indirectly through Tri-IPCs. Immunostaining further validated these results (Extended Data Fig. 12a–f).

The lineage tracing experiments described so far were conducted at the population level. To assess the lineage potential of glial progenitors at the single-cell level, we isolated individual RG-tRGs, RG-oRGs, and Tri-IPCs and cultured them for 14 days to produce clonal descendants. For both RG-tRGs and RG-oRGs, 5 out of 10 clones contained both IPC-ENs and Tri-IPCs, illustrating that individual RGs can generate both cell types (Fig. 4d). Moreover, 7 out of 10 Tri-IPC clones contained astrocytes, OPCs, and INs, confirming the tripotential nature of individual Tri-IPCs (Fig. 4d). Additionally, we transplanted isolated glial progenitors onto cultured human cortical slices ex vivo to provide a more physiologically relevant environment (Extended Data

11

333 Fig. 12g). Consistent with our in vitro findings, RGs predominantly produced IPC-ENs within 8
334 days, whereas Tri-IPCs produced astrocytes, OPCs, and INs (Fig. 4f, Extended Data Fig. 12h–j).

335 To determine the specific subtype of INs produced by Tri-IPCs, we obtained scRNA-seq data
336 from human ganglionic eminence as a reference[44] and annotated interneuron subtypes based on
337 marker genes reported in the literature[45] (Extended Data Fig. 13a,b). We then trained a random-
338 forest-based classifier using SingleCellNet[46] based on this reference dataset, revealing that INs
339 derived from Tri-IPCs closely resembled $MEIS2^+PAX6^+$ INs from dLGE and CGE (Fig. 4f).
340 These cells were also $SP8^+SCGN^+$ and were projected to develop into olfactory bulb interneurons
341 and white matter interneurons[45]. This aligns with the presence of Tri-IPCs and IN-dLGE-
342 Immatures in the white matter of both prenatal and postnatal human telencephalon observed in
343 our MERFISH data (Extended Data Fig. 5a–f) and suggests that some of these IN-dLGE-
344 Immatures may originate from Tri-IPCs. Similar results were obtained with a nearest-neighbor-
345 based label transfer approach using Seurat (Fig. 4f, Extended Data Fig. 13c,d). Additionally, we
346 aimed to categorize the types of astrocytes derived from Tri-IPCs. A recent study delineated two
347 lineage origins of astrocytes in the mouse neocortex—an Olig2 lineage primarily producing gray
348 matter or protoplasmic astrocytes and an S100a11 lineage primarily producing white matter or
349 fibrous astrocytes[47]. We applied similar classification analysis using scRNA-seq data from the
350 developing mouse neocortex[48] and human snMultiome data from this study as references
351 (Extended Data Fig. 13e,f,i,j). We found that Tri-IPC-derived astrocytes were mapped to both
352 Olig2 and S100a11 lineages, indicating their potential to produce both protoplasmic and fibrous
353 astrocytes (Fig. 4f, Extended Data Fig. 13g,h,k,l). Based on these results, we propose an updated
354 model of the origin and lineage potential of human neural progenitors in the late second trimester
355 (Fig. 4g).

356 ### *Cell type relevance to human cognition and brain disorders*

357 Approximately 90% of variants identified in genome-wide association studies (GWASs) were
358 found within non-protein-coding regions of the genome[49,50]. Leveraging the chromatin
359 accessibility data we obtained from the developing human neocortex, we applied SCAVENGE[51]
360 to map GWAS variants to their relevant cellular context at single-cell resolution. Specifically, the
361 algorithm quantifies the enrichment of GWAS variants within the open chromatin regions of a
362 cell and overcomes the sparsity issue of single-cell profiles via network propagation. The
363 enrichment strength was quantified by trait-relevance scores (TRSs) at the single-cell level and
364 the proportion of significantly enriched cells at the cell-group level. Using this approach, we
365 analyzed four cognitive traits and five neuropsychiatric disorders, revealing that they all had
366 significant associations with specific cell types (Fig. 5a–c, Supplementary Table 17). Concerning
367 cognitive traits, we found that fluid intelligence and processing speed were associated with IT
368 neurons, aligning with previous results in the adult human brain (Fig. 5a,c) [34]. In addition, we
369 were surprised to observe an association between RGs and executive function and between
370 microglia and working memory (Fig. 5a,c). The exact mechanisms underlying these associations
371 remain to be elucidated. Regarding psychiatric disorders, all exhibited significant associations
372 with various types of ENs (Fig. 5b,c). Bipolar disorder (BPD), schizophrenia (SCZ), and
373 attention-deficit/hyperactivity disorder (ADHD), but not autism spectrum disorder (ASD) or
374 major depressive disorder (MDD), were additionally linked to INs (Fig. 5b,c), highlighting
375 differential disease association between the two major neuronal subclasses. Notably, some of the
376 strongest associations were found between ASD and specific IT types (EN-IT-Immatures and
377 EN-L6-ITs). As a control, we evaluated the association between neocortical cell types and
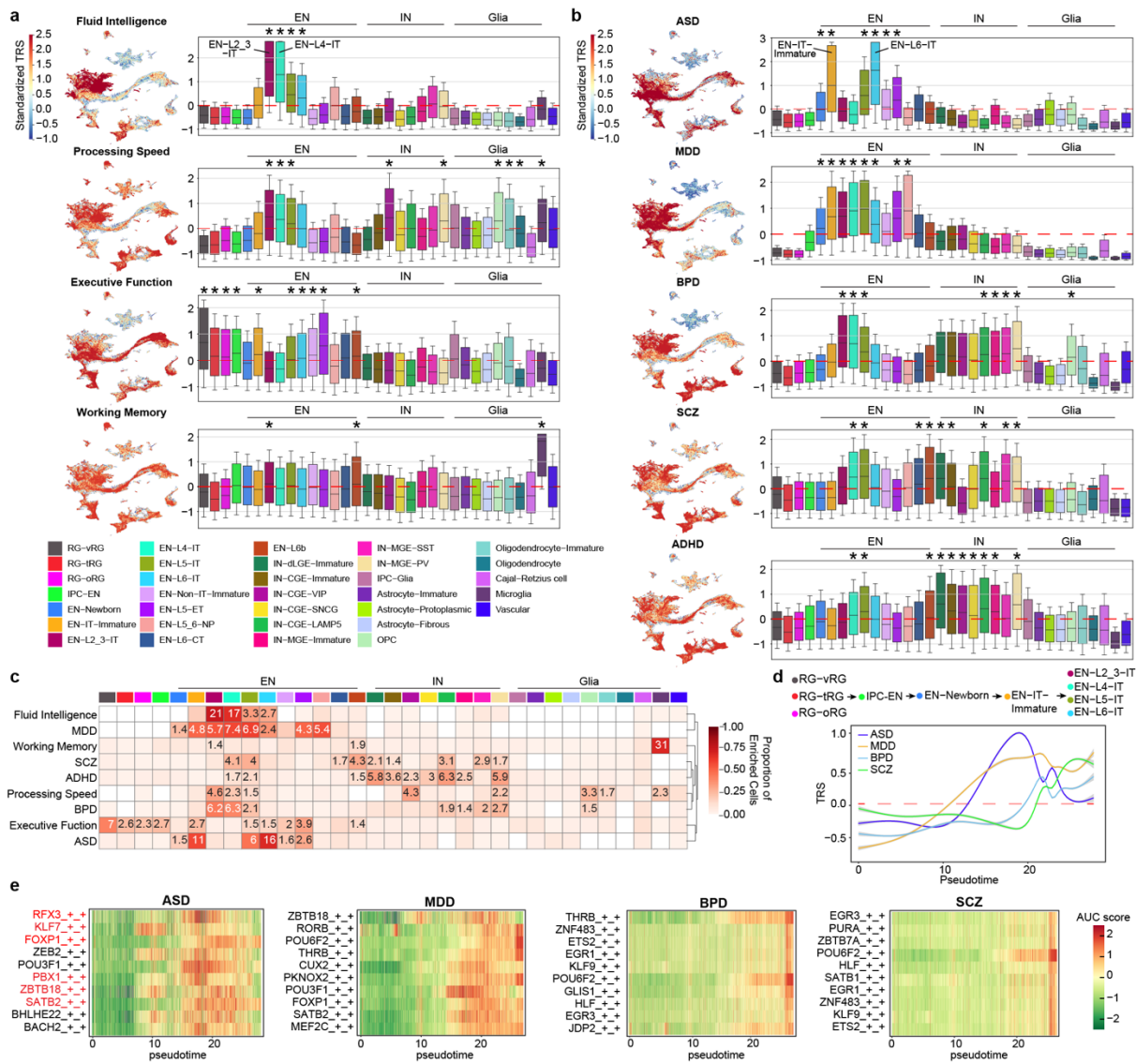
**Fig. 5. | Cell type association with human cognition and brain disorders. a**, Standardized per-cell SCAVENGE trait relevance score (TRS) for four cognitive functions. Boxplot center: median; hinges: the 25th and 75th percentiles; whiskers: standard error. **b**, Standardized per-cell SCAVENGE TRS for five brain disorders, including autism spectrum disorder (ASD), major depressive disorder (MDD), bipolar disorder (BPD), attention-deficit/hyperactivity disorder (ADHD), and schizophrenia (SCZ). Boxplot center: median; hinges: the 25th and 75th percentiles; whiskers: standard error. Hypergeometric test, *FDR < 0.01 & odds ratio > 1.4. **c**, Heatmap showing the proportion of the cells with enriched trait relevance across cell types. Tiles with significant TRS enrichment (hypergeometric test, *FDR < 0.01 & odds ratio > 1.4) are annotated by their odd ratios. **d**, Standardized SCAVENGE TRS of four brain disorders plotted along the intratelencephalic (IT) neuron lineage pseudotime. The best-fitted smoothed lines indicate the average TRS and the 95% confidence interval in each pseudo-time bin. **e**, Heatmaps of standardized gene-based AUC scores for top ten disease-relevant eRegulons ranked by Spearman's ρ along the IT neuron lineage pseudotime. eRegulons with SFARI ASD-associated genes as core TFs are highlighted in red.

378  Alzheimer's disease, which is known to have a strong heritability component in microglia[52,53].
379  We not only observed the strongest enrichment of Alzheimer's disease-associated variants in
380  microglia but also identified significant enrichment in vascular cells and astrocytes (Extended
381  Data Fig. 14a,b), consistent with their involvement in the disease[54,55]. It is important to note that

13

382 our analysis was based on common variants and may not uncover contributions from other cell
383 types due to the involvement of rare variants or environmental factors.

384 Besides cell types, we also compared trait associations among brain regions and age groups,
385 revealing that differences between age groups were more pronounced than between regions
386 (Extended Data Fig. 14c–f, Supplementary Table 18). For example, risk variants associated with
387 neuropsychiatric disorders displayed distinct patterns of enrichment across age groups, with ASD
388 risk enrichment peaking in the second trimester (Extended Data Fig. 14e–f). Given the
389 predominant enrichment of these risk variants in ENs (Fig. 5b,c), we postulated that they target
390 distinct stages of EN differentiation and maturation. To test this hypothesis, we selected EN
391 lineage cells and examined the patterns of TRSs along their pseudotime (Fig. 5d). Indeed, ASD
392 showed the earliest TRS peak, followed by MDD, BPD, and SCZ. This pattern is consistent with
393 the earlier onset of ASD compared to other disorders and explains why previous heritability
394 analyses of ASD in the adult brain found only a modest signal in ENs[34]. To pinpoint potential
395 gene regulatory networks disrupted by disease risk variants during EN differentiation, we
396 identified eRegulons whose activity positively correlated with the TRSs for each disorder (Fig.
397 5e, Supplementary Table 19). Among the core TFs of the top ten eRegulons correlated with ASD,
398 six were recognized as ASD risk genes and listed in the SFARI gene database[56]. Together, our
399 analysis not only pinpointed the most relevant cell types and developmental stages for cognitive
400 traits and brain disorders but also elucidated potential disease mechanisms at cellular and
401 molecular levels.

402 **Discussion**

403 In this study, we extensively characterized the developing human neocortex in multiple stages,
404 regions, and across multiple dimensions, including transcriptomic, epigenomic, spatial, and
405 functional analyses. These data collectively establish an atlas of the human neocortex in various
406 developmental stages at single-cell resolution. The integration of multi-omic data has provided
407 insights into diverse aspects, including cellular composition, spatial organization, gene regulatory
408 networks, lineage potential, and susceptibility to diseases during brain development. By
409 combining spatial and snMultiome data, we further elucidate intricate cell-cell communication
410 networks during development, emphasizing robust interactions between EN and IN subclasses
411 mediated by specific signaling pathways.

412 V1 in humans, primates, and other binocular mammals exhibits a specialized cytoarchitecture
413 characterized by an enlarged layer 4 that receives inputs from the thalamus[57]. Recent brain cell
414 census studies in humans and non-human primates have identified a distinct population of EN-
415 L4-ITs exclusively present in V1[19,58]. However, the mechanisms responsible for their emergence
416 and the factors determining their identity have been unknown. Our results suggest that common
417 and V1-specific EN-L4-ITs initially share a common developmental trajectory until the third
418 trimester, after which they diverge. Common EN-L4-ITs follow a trajectory similar to that of
419 EN-L5-IT, whereas V1-specific EN-L4-ITs partially share a trajectory with EN-L2_3-IT.
420 Furthermore, we have identified TFs and eRegulons responsible for V1-specific EN-L4-ITs
421 differentiation, including *SMAD3*, *GLIS3*, and *CUX2* at early stages, as well as *POU6F2*, *JDP2*,
422 and *CUX1* at later stages. These results elucidate genetic programs governing sequential neuronal
423 fate determination. They also offer crucial insights and serve as a benchmark for the future
424 development of area-specific in vitro models of human cortical development.

Previous studies in rodents have demonstrated that following the peak neurogenesis of ENs, RGs within the dorsal telencephalon gradually transition to gliogenesis. Concurrently, they begin transitioning into a specific subtype of adult VZ/SVZ stem cells that produces olfactory bulb interneurons[59–61]. In humans and other non-human primates, however, a longstanding debate persists concerning two fundamental questions: firstly, whether cortical progenitors, particularly cortical RGs, have the capacity to generate INs during embryonic development, and secondly, what subtype of neurons these INs eventually mature into[62–66]. Regarding the first question, most evidence supporting the "local production" hypothesis focuses primarily on identifying IN progenitors in the cortex, albeit failing to conclusively rule out the possibility that these IN progenitors originate in the ventral telencephalon[67]. Recently, we and others have demonstrated that cortical RGs in the second trimester can produce LGE- and CGE-like INs that share a lineage with ENs[43,68]. However, whether these INs are generated directly from RGs or indirectly via IPCs remained uncertain. In this study, we observed that both oRGs and tRGs give rise to INs through tripotential IPCs, which we named Tri-IPCs. Based on the expression of EGFR and OLIG2, human Tri-IPCs likely correspond to "MIPCs" found in mice[42] and proposed in humans[38]. The onset of Tri-IPC production occurs in the late second trimester (after gestational week 18), potentially due to increased sonic hedgehog signaling during later stages of cortical development[69–71]. These findings provide an explanation for the limited production of INs observed in short-term cultures of human organotypic slices before gestational week 18[64].

Concerning the identity of INs born in the cortex, our classification suggests that the vast majority of Tri-IPC-derived INs are transcriptomically similar to $MEIS2^+PAX6^+$ INs presumed to originate from the dLGE[45]. Interestingly, these INs are also found in scRNA-seq data from the CGE[44], consistent with that $MEIS2^+$ cells have been observed in the CGE[72]. Moreover, $MEIS2^+PAX6^+$ INs emerge in dorsally patterned human cerebral organoids, particularly at their later developmental stages[43]. Thus, instead of an IN type whose origin is confined to the LGE, we propose that $MEIS2^+PAX6^+$ INs represent the most dorsal type of IN generated within the germinal zone of the cortex and its neighboring ganglionic eminence. In mice, INs derived from MIPCs were reported to differentiate into olfactory bulb interneurons [42]. However, our spatial transcriptomic data demonstrate the presence of $MEIS2^+PAX6^+$ INs in the white matter of both prenatal and postnatal human brain, indicating their potential role as white matter interneurons. With recent reports of a shared origin between some cortical interneurons and ENs[73,74], it remains to be determined whether INs derived from Tri-IPCs also differentiate into cortical interneurons.

Most genetic risk for ASD comes from common variants found in non-coding regions of the genome[75]. However, understanding the underlying cellular and molecular mechanisms has remained challenging due to a lack of comprehensive cell-type-resolved epigenomic data from the developing human brain. Our variant mapping at single-cell resolution reveals pronounced enrichment of ASD-linked common risk variants within chromatin-accessible regions specific to IT neurons in the second trimester, aligning with ASD as a neurodevelopmental disorder primarily originating at midgestation. The relevance of midgestational cortical development to ASD is further supported by data from gene expression analysis of both common and rare de novo ASD variants[76–78]. Moreover, our analyses indicate that disrupting cortical-cortical connectivity, particularly by impacting IT neurons in early development, may contribute to ASD pathophysiology. Notably, EN-IT-Immatures in the second trimester differentiate predominantly into EN-L2_3-ITs and EN-L4-ITs postnatally. Intriguingly, EN-L2_3-ITs and EN-L4-ITs are among the most affected cell types in post-mortem ASD brain[79], highlighting how early-acting

15

471    ASD risk variants cascade into postnatal deficits within IT neurons. Our analysis extends beyond
472    ASD and reveals temporal- and cell-type-specific risk patterns associated with multiple brain
473    disorders. For example, ASD exhibits the earliest risk, succeeded by MDD, and then followed by
474    BPD and SCZ. Moreover, BPD, SCZ, and ADHD, but not ASD or MDD, were linked to
475    inhibitory neurons. These findings underscore the significance of studying the typical trajectory
476    of brain development in understanding the deviations leading to specific diseases.

## Reference

1. Molnár, Z. *et al.* New insights into the development of the human cerebral cortex. *J Anat* **235**, 432–451 (2019).

2. Long, H. K., Prescott, S. L. & Wysocka, J. Ever-Changing Landscapes: Transcriptional Enhancers in Development and Evolution. *Cell* **167**, 1170–1187 (2016).

3. Nowakowski, T. J. *et al.* Spatiotemporal gene expression trajectories reveal developmental hierarchies of the human cortex. *Science* **358**, 1318–1323 (2017).

4. Zhong, S. *et al.* A single-cell RNA-seq survey of the developmental landscape of the human prefrontal cortex. *Nature* **555**, 524–528 (2018).

5. Li, M. *et al.* Integrative functional genomic analysis of human brain development and neuropsychiatric risks. *Science* **362**, eaat7615 (2018).

6. Polioudakis, D. *et al.* A Single-Cell Transcriptomic Atlas of Human Neocortical Development during Mid-gestation. *Neuron* **103**, 785-801.e8 (2019).

7. Fan, X. *et al.* Single-cell transcriptome analysis reveals cell lineage specification in temporal-spatial patterns in human cortical development. *Sci Adv* **6**, eaaz2978 (2020).

8. Eze, U. C., Bhaduri, A., Haeussler, M., Nowakowski, T. J. & Kriegstein, A. R. Single-cell atlas of early human brain development highlights heterogeneity of human neuroepithelial cells and early radial glia. *Nat Neurosci* **24**, 584–594 (2021).

9. Bhaduri, A. *et al.* An atlas of cortical arealization identifies dynamic molecular signatures. *Nature* **598**, 200–204 (2021).

10. Braun, E. *et al.* Comprehensive cell atlas of the first-trimester developing human brain. *Science* **382**, eadf1226 (2023).

11. Velmeshev, D. *et al.* Single-cell analysis of prenatal and postnatal human cortical development. *Science* **382**, eadf0834 (2023).

12. Ramos, S. I. *et al.* An atlas of late prenatal human neurodevelopment resolved by single-nucleus transcriptomics. *Nat Commun* **13**, 7671 (2022).

13. Li, Y. *et al.* Spatiotemporal transcriptome atlas reveals the regional specification of the developing human brain. *Cell* **186**, 5892-5909.e22 (2023).

14. Ziffra, R. S. *et al.* Single-cell epigenomics reveals mechanisms of human cortical development. *Nature* **598**, 205–213 (2021).

15. Trevino, A. E. *et al.* Chromatin and gene-regulatory dynamics of the developing human cerebral cortex at single-cell resolution. *Cell* **184**, 5053-5069.e23 (2021).

16. van Bruggen, D. *et al.* Developmental landscape of human forebrain at a single-cell level identifies early waves of oligodendrogenesis. *Dev Cell* **57**, 1421-1436.e5 (2022).

17. Zhu, K. *et al.* Multi-omic profiling of the developing human cerebral cortex at the single-cell level. *Sci Adv* **9**, eadg3754 (2023).

18. Hao, Y. *et al.* Integrated analysis of multimodal single-cell data. *Cell* **184**, 3573-3587.e29 (2021).

19. Jorstad, N. L. *et al.* Transcriptomic cytoarchitecture reveals principles of human neocortex organization. *Science* **382**, eadf6812 (2023).

20. Bishop, K. M., Goudreau, G. & O'Leary, D. D. M. Regulation of area identity in the mammalian neocortex by Emx2 and Pax6. *Science* **288**, 344–349 (2000).

519  21.  Chen, K. H., Boettiger, A. N., Moffitt, J. R., Wang, S. & Zhuang, X. Spatially resolved, highly
520       multiplexed RNA profiling in single cells. *Science* **348**, aaa6090 (2015).

521  22.  Lim, L., Mi, D., Llorca, A. & Marín, O. Development and Functional Diversification of
522       Cortical Interneurons. *Neuron* **100**, 294–313 (2018).

523  23.  Stenman, J., Toresson, H. & Campbell, K. Identification of Two Distinct Progenitor
524       Populations in the Lateral Ganglionic Eminence: Implications for Striatal and Olfactory
525       Bulb Neurogenesis. *Journal of Neuroscience* **23**, 167–174 (2003).

526  24.  Akay, L. A., Effenberger, A. H. & Tsai, L. H. Cell of all trades: oligodendrocyte precursor
527       cells in synaptic, vascular, and immune function. *Genes Dev* **35**, 180–198 (2021).

528  25.  Mittelbronn, M., Dietz, K., Schluesener, H. J. & Meyermann, R. Local distribution of
529       microglia in the normal adult human central nervous system differs by up to one order of
530       magnitude. *Acta Neuropathol* **101**, 249–255 (2001).

531  26.  Kriegstein, A. & Alvarez-Buylla, A. The Glial Nature of Embryonic and Adult Neural Stem
532       Cells. *Annu Rev Neurosci* **32**, 149–184 (2009).

533  27.  Brill, M. S. *et al.* Adult generation of glutamatergic olfactory bulb interneurons. *Nature
534       Neuroscience 2009 12:12* **12**, 1524–1533 (2009).

535  28.  Fischer, D. S., Schaar, A. C. & Theis, F. J. Modeling intercellular communication in tissues
536       using spatial graphs of cells. *Nature Biotechnology 2022 41:3* **41**, 332–336 (2022).

537  29.  Jin, S. *et al.* Inference and analysis of cell-cell communication using CellChat. *Nat
538       Commun* **12**, 1–20 (2021).

539  30.  Bravo González-Blas, C. *et al.* SCENIC+: single-cell multiomic inference of enhancers and
540       gene regulatory networks. *Nature Methods 2023 20:9* **20**, 1355–1367 (2023).

541  31.  Aibar, S. *et al.* SCENIC: Single-cell regulatory network inference and clustering. *Nat
542       Methods* **14**, 1083–1086 (2017).

543  32.  Street, K. *et al.* Slingshot: Cell lineage and pseudotime inference for single-cell
544       transcriptomics. *BMC Genomics* **19**, 1–16 (2018).

545  33.  Van den Berge, K. *et al.* Trajectory-based differential expression analysis for single-cell
546       sequencing data. *Nat Commun* **11**, 1–13 (2020).

547  34.  Li, Y. E. *et al.* A comparative atlas of single-cell chromatin accessibility in the human brain.
548       *Science* **382**, eadf7044 (2023).

549  35.  Cadwell, C. R., Bhaduri, A., Mostajo-Radji, M. A., Keefe, M. G. & Nowakowski, T. J.
550       Development and Arealization of the Cerebral Cortex. *Neuron* **103**, 980–1004 (2019).

551  36.  Huang, W. *et al.* Origins and Proliferative States of Human Oligodendrocyte Precursor
552       Cells. *Cell* **182**, 594-608.e11 (2020).

553  37.  Fu, Y. *et al.* Heterogeneity of glial progenitor cells during the neurogenesis-to-gliogenesis
554       switch in the developing human cerebral cortex. *Cell Rep* **34**, 108788 (2021).

555  38.  Yang, L., Li, Z., Liu, G., Li, X. & Yang, Z. Developmental Origins of Human Cortical
556       Oligodendrocytes and Astrocytes. *Neurosci Bull* **38**, 47–68 (2022).

557  39.  Liu, D. D. *et al.* Purification and characterization of human neural stem and progenitor
558       cells. *Cell* **186**, 1179-1194.e15 (2023).

559  40.  Weng, Q. *et al.* Single-Cell Transcriptomics Uncovers Glial Progenitor Diversity and Cell
560       Fate Determinants during Development and Gliomagenesis. *Cell Stem Cell* **24**, 707-723.e8
561       (2019).

41. Zhang, Y. *et al.* Cortical Neural Stem Cell Lineage Progression Is Regulated by Extrinsic Signaling Molecule Sonic Hedgehog. *Cell Rep* **30**, 4490-4504.e4 (2020).

42. Li, X. *et al.* Decoding Cortical Glial Cell Development. *Neurosci Bull* **37**, 440–460 (2021).

43. Andrews, M. G. *et al.* LIF signaling regulates outer radial glial to interneuron fate during human cortical development. *Cell Stem Cell* **30**, 1382-1391.e5 (2023).

44. Shi, Y. *et al.* Mouse and human share conserved transcriptional programs for interneuron development. *Science* **374**, eabj6641 (2021).

45. Schmitz, M. T. *et al.* The development and evolution of inhibitory neurons in primate cerebrum. *Nature* **603**, 871–877 (2022).

46. Tan, Y. & Cahan, P. SingleCellNet: A Computational Tool to Classify Single Cell RNA-Seq Data Across Platforms and Across Species. *Cell Syst* **9**, 207-213.e2 (2019).

47. Zhou, J. *et al.* Dual lineage origins of neocortical astrocytes. *bioRxiv* 2023.09.12.557313 (2023) doi:10.1101/2023.09.12.557313.

48. Di Bella, D. J. *et al.* Molecular logic of cellular diversification in the mouse cerebral cortex. *Nature* **595**, 554–559 (2021).

49. Edwards, S. L., Beesley, J., French, J. D. & Dunning, M. Beyond GWASs: Illuminating the Dark Road from Association to Function. *The American Journal of Human Genetics* **93**, 779–797 (2013).

50. Finucane, H. K. *et al.* Partitioning heritability by functional annotation using genome-wide association summary statistics. *Nature Genetics 2015 47:11* **47**, 1228–1235 (2015).

51. Yu, F. *et al.* Variant to function mapping at single-cell resolution through network propagation. *Nature Biotechnology 2022 40:11* **40**, 1644–1653 (2022).

52. Nott, A. *et al.* Brain cell type–specific enhancer–promoter interactome maps and disease-risk association. *Science* **366**, 1134–1139 (2019).

53. Corces, M. R. *et al.* Single-cell epigenomic analyses implicate candidate causal variants at inherited risk loci for Alzheimer's and Parkinson's diseases. *Nat Genet* **52**, 1158–1168 (2020).

54. Yang, A. C. *et al.* A human brain vascular atlas reveals diverse mediators of Alzheimer's risk. *Nature* **603**, 885–892 (2022).

55. Arranz, A. M. & De Strooper, B. The role of astroglia in Alzheimer's disease: pathophysiology and clinical implications. *Lancet Neurol* **18**, 406–414 (2019).

56. Abrahams, B. S. *et al.* SFARI Gene 2.0: A community-driven knowledgebase for the autism spectrum disorders (ASDs). *Mol Autism* **4**, 1–3 (2013).

57. Harumi Yabuta, N. & Callaway, E. M. Functional Streams and Local Connections of Layer 4C Neurons in Primary Visual Cortex of the Macaque Monkey. *Journal of Neuroscience* **18**, 9489–9499 (1998).

58. Krienen, F. M. *et al.* A marmoset brain cell census reveals regional specialization of cellular identities. *Sci Adv* **9**, eadk3986 (2023).

59. Kohwi, M. *et al.* A Subpopulation of Olfactory Bulb GABAergic Interneurons Is Derived from Emx1- and Dlx5/6-Expressing Progenitors. *Journal of Neuroscience* **27**, 6878–6891 (2007).

60. Young, K. M., Fogarty, M., Kessaris, N. & Richardson, W. D. Subventricular Zone Stem Cells Are Heterogeneous with Respect to Their Embryonic Origins and Neurogenic Fates in the Adult Olfactory Bulb. *Journal of Neuroscience* **27**, 8286–8296 (2007).

61. Fuentealba, L. C. *et al.* Embryonic Origin of Postnatal Neural Stem Cells. *Cell* **161**, 1644–1655 (2015).

62. Joyce, A. *et al.* Origin of GABAergic neurons in the human neocortex. *Nature* **417**, 645–649 (2002).

63. Zecevic, N., Hu, F. & Jakovcevski, I. Interneurons in the developing human neocortex. *Dev Neurobiol* **71**, 18–33 (2011).

64. Hansen, D. V. *et al.* Non-epithelial stem cells and cortical interneuron production in the human ganglionic eminences. *Nat Neurosci* **16**, 1576–1587 (2013).

65. Ma, T. *et al.* Subcortical origins of human and monkey neocortical interneurons. *Nature Neuroscience 2013 16:11* **16**, 1588–1597 (2013).

66. Alzu'Bi, A. *et al.* The Transcription Factors COUP-TFI and COUP-TFII have Distinct Roles in Arealisation and GABAergic Interneuron Specification in the Early Human Fetal Telencephalon. *Cerebral Cortex* **27**, 4971–4987 (2017).

67. Wu, S. *et al.* Tangential migration and proliferation of intermediate progenitors of GABAergic neurons in the mouse telencephalon. *Development* **138**, 2499–2509 (2011).

68. Delgado, R. N. *et al.* Individual human cortical progenitors can produce excitatory and inhibitory neurons. *Nature* **601**, 397–403 (2021).

69. Dahmane, N. *et al.* The Sonic Hedgehog-Gli pathway regulates dorsal brain growth and tumorigenesis. *Development* **128**, 5201–5212 (2001).

70. Ortega, J. A., Radonjić, N. V. & Zecevic, N. Sonic hedgehog promotes generation and maintenance of human forebrain Olig2 progenitors. *Front Cell Neurosci* **7**, 62556 (2013).

71. Zhang, Y. *et al.* Cortical Neural Stem Cell Lineage Progression Is Regulated by Extrinsic Signaling Molecule Sonic Hedgehog. *Cell Rep* **30**, 4490-4504.e4 (2020).

72. Yu, Y. *et al.* Interneuron origin and molecular diversity in the human fetal brain. *Nat Neurosci* **24**, 1745–1756 (2021).

73. Chung, C. *et al.* Cell-type-resolved somatic mosaicism reveals clonal dynamics of the human forebrain. *bioRxiv* 2023.10.24.563814 (2023) doi:10.1101/2023.10.24.563814.

74. Kim, S. N. *et al.* Cell lineage analysis with somatic mutations reveals late divergence of neuronal cell types and cortical areas in human cerebral cortex. *bioRxiv* 2023.11.06.565899 (2023) doi:10.1101/2023.11.06.565899.

75. Gaugler, T. *et al.* Most genetic risk for autism resides with common variation. *Nature Genetics 2014 46:8* **46**, 881–885 (2014).

76. Grove, J. *et al.* Identification of common genetic risk variants for autism spectrum disorder. *Nature Genetics 2019 51:3* **51**, 431–444 (2019).

77. Parikshak, N. N. *et al.* Integrative functional genomic analyses implicate specific molecular pathways and circuits in autism. *Cell* **155**, 1008 (2013).

78. Willsey, A. J. *et al.* Coexpression Networks Implicate Human Midfetal Deep Cortical Projection Neurons in the Pathogenesis of Autism. *Cell* **155**, 997–1007 (2013).

79. Velmeshev, D. *et al.* Single-cell genomics identifies cell type-specific molecular changes in autism. *Science* **364**, 685–689 (2019).

80. Wang, L. & Kriegstein, A. Nuclei Isolation from Tissue for 10x Multiome by Iodixanol. *protocol.io* (2023) doi:10.17504/PROTOCOLS.IO.EQ2LYJ3NPLX9/V1.

81. Wolock, S. L., Lopez, R. & Klein, A. M. Scrublet: Computational Identification of Cell Doublets in Single-Cell Transcriptomic Data. *Cell Syst* **8**, 281-291.e9 (2019).

650  82.  Zhang, Y. *et al.* Model-based analysis of ChIP-Seq (MACS). *Genome Biol* **9**, R137 (2008).

651  83.  Amemiya, H. M., Kundaje, A. & Boyle, A. P. The ENCODE Blacklist: Identification of
652       Problematic Regions of the Genome. *Sci Rep* **9**, (2019).

653  84.  Stuart, T., Srivastava, A., Madad, S., Lareau, C. A. & Satija, R. Single-cell chromatin state
654       analysis with Signac. *Nature Methods 2021 18:11* **18**, 1333–1341 (2021).

655  85.  Choudhary, S. & Satija, R. Comparison and evaluation of statistical error models for
656       scRNA-seq. *Genome Biol* **23**, 27 (2022).

657  86.  Butler, A., Hoffman, P., Smibert, P., Papalexi, E. & Satija, R. Integrating single-cell
658       transcriptomic data across different conditions, technologies, and species. *Nat Biotechnol*
659       **36**, 411–420 (2018).

660  87.  Waltman, L. & Van Eck, N. J. A smart local moving algorithm for large-scale modularity-
661       based community detection. *Eur Phys J B* **86**, 471 (2013).

662  88.  Phipson, B. *et al.* propeller: testing for differences in cell type proportions in single cell
663       data. *Bioinformatics* **38**, 4720–4726 (2022).

664  89.  Ritchie, M. E. *et al.* limma powers differential expression analyses for RNA-sequencing
665       and microarray studies. *Nucleic Acids Res* **43**, e47–e47 (2015).

666  90.  Schep, A. N., Wu, B., Buenrostro, J. D. & Greenleaf, W. J. chromVAR: inferring
667       transcription-factor-associated accessibility from single-cell epigenomic data. *Nat*
668       *Methods* **14**, 975–978 (2017).

669  91.  Fornes, O. *et al.* JASPAR 2020: update of the open-access database of transcription factor
670       binding profiles. *Nucleic Acids Res* **48**, D87–D92 (2020).

671  92.  Hao, Y. *et al.* Dictionary learning for integrative, multimodal and scalable single-cell
672       analysis. *Nat Biotechnol* (2023) doi:10.1038/s41587-023-01767-y.

673  93.  Nguyen, L. Van *et al.* Fast unfolding of communities in large networks. *Journal of*
674       *Statistical Mechanics: Theory and Experiment* **2008**, P10008 (2008).

675  94.  Palla, G. *et al.* Squidpy: a scalable framework for spatial omics analysis. *Nature Methods*
676       *2022 19:2* **19**, 171–178 (2022).

677  95.  Hie, B., Cho, H., DeMeo, B., Bryson, B. & Berger, B. Geometric Sketching Compactly
678       Summarizes the Single-Cell Transcriptomic Landscape. *Cell Syst* **8**, 483-493.e7 (2019).

679  96.  Bravo González-Blas, C. *et al.* cisTopic: cis-regulatory topic modeling on single-cell ATAC-
680       seq data. *Nat Methods* **16**, 397–400 (2019).

681  97.  Janky, R. *et al.* iRegulon: From a Gene List to a Gene Regulatory Network Using Large
682       Motif and Track Collections. *PLoS Comput Biol* **10**, e1003731 (2014).

683  98.  Van de Sande, B. *et al.* A scalable SCENIC workflow for single-cell gene regulatory network
684       analysis. *Nat Protoc* **15**, 2247–2276 (2020).

685  99.  Scrucca, L., Fraley, C., Murphy, T. B. & Raftery, A. E. *Model-Based Clustering, Classification,*
686       *and Density Estimation Using mclust in R*. *Model-Based Clustering, Classification, and*
687       *Density Estimation Using mclust in R* (CRC Press, 2023). doi:10.1201/9781003277965.

688  100. Yu, G., Wang, L. G., Han, Y. & He, Q. Y. ClusterProfiler: An R package for comparing
689       biological themes among gene clusters. *OMICS* **16**, 284–287 (2012).

690  101. Rivellese, F. *et al.* Rituximab versus tocilizumab in rheumatoid arthritis: synovial biopsy-
691       based biomarker analysis of the phase 4 R4RA randomized trial. *Nat Med* **28**, 1256–1268
692       (2022).

693    102.   Robinson, M. D., McCarthy, D. J. & Smyth, G. K. edgeR: A Bioconductor package for
694            differential expression analysis of digital gene expression data. *Bioinformatics* **26**, 139–
695            140 (2009).
696    103.   Schindelin, J. *et al.* Fiji: An open-source platform for biological-image analysis. *Nat*
697            *Methods* **9**, 676–682 (2012).
698    104.   Ulirsch, J. C. *et al.* Interrogation of human hematopoiesis at single-cell and single-variant
699            resolution. *Nature Genetics 2019 51:4* **51**, 683–693 (2019).
700
701

**Methods**

Brain tissue samples

Human brain tissue samples (Supplementary Table 1 and 5) were acquired from four different sources.

Four de-identified first-trimester human tissue samples were collected from the Human Developmental Biology Resource (HDBR), staged using crown-rump length and snap-frozen on dry ice. After tissue acquisition, the cortical plate and subplate were dissected and frozen at −80 °C.

Thirteen de-identified second-trimester human tissue samples were collected at the Zuckerberg San Francisco General Hospital (ZSFGH). Acquisition of second-trimester human tissue samples was approved by the UCSF Human Gamete, Embryo and Stem Cell Research Committee (study number 10-05113). All experiments were performed in accordance with protocol guidelines. Informed consent was obtained before sample collection and use for this study.

Two de-identified third-trimester and early postnatal tissue samples were obtained at the UCSF Pediatric Neuropathology Research Laboratory (PNRL) led by Dr. Eric Huang. These samples were acquired with patient consent in strict observance of the legal and institutional ethical regulations and in accordance with research protocols approved by the UCSF IRB committee. These samples were dissected and snap-frozen either on a cold plate placed on a slab of dry ice or in isopentane on dry ice.

Twenty-three de-identified third trimester, early postnatal, and adolescent tissue samples without known neurological disorders were obtained from the University of Maryland Brain and Tissue Bank through NIH NeuroBioBank.

Samples used for single-nucleus analysis were listed in Supplementary Table 1, and those for spatial transcriptomic analysis were listed in Supplementary Table 5.


Nuclei isolation and generation of single-nucleus multiome (snMultiome) data

Detailed protocol can be found at ref[80]. All procedures were done on ice or at 4°C. Briefly, frozen tissue samples (20–50 mg) were homogenized using a pre-chilled 7 ml Dounce homogenizer containing 1 ml cold homogenization buffer (HB) (20 mM Tricine-KOH pH 7.8, 250 mM sucrose, 25 mM KCl, 5 mM $MgCl_2$, 1 mM dithiothreitol, 0.5 mM Spermidine, 0.5 mM Spermine, 0.3% NP-40, 1× cOmplete protease inhibitor [Roche], and 0.6 U/mL RiboLock [Thermo Fisher]). The tissue samples were homogenized 10 times with the loose pestle and 15 times with the tight pestle. Nuclei were pelleted by spinning at 350 × g for 5 min, resuspended in 25% iodixanol solution, and loaded onto 30% and 40% iodixanol layers to make a gradient. The gradient was spun at 3,000 × g for 20 min. Clean nuclei were collected at the 30%–40% interface and diluted in wash buffer (10 mM Tris-HCl pH 7.4, 10 mM NaCl, 3 mM $MgCl_2$, 1 mM dithiothreitol, 1% BSA, 0.1% Tween 20, and 0.6 U/mL RiboLock [Thermo Fisher]). Next, nuclei were pelleted by spinning at 500 × g for 5 min and resuspended in diluted nuclei buffer (10X Genomics). Nuclei were counted using a hemocytometer, diluted to 3220 nuclei/μL, and further processed following 10X Genomics Chromium Next GEM Single Cell Multiome ATAC + Gene Expression Reagent Kits user guide. We targeted 10,000 nuclei per sample per reaction. Libraries from individual samples were pooled and sequenced on the NovaSeq 6000 sequencing system, targeting 25,000 read pairs per nucleus for ATAC and 25,000 read pairs for RNA.

23

744

## snMultiome data pre-processing

746 The raw sequencing signals in the BCL format were demultiplexed into fastq format using the
747 "mkfastq" function in the Cell Ranger ARC suite (v.2.0.0, 10x Genomics). Cell Ranger-ARC count
748 pipeline was implemented for cell barcode calling, reads alignment, and quality assessment using
749 the human reference genome (GRCh38) following the protocols described by 10X Genomics. The
750 pipeline assessed the overall quality to retain all intact nuclei from the background and filtered out
751 non-nucleus-associated reads. All gene expression libraries in this study showed a high fraction of
752 reads in nuclei, indicating high RNA content in called nuclei and minimal levels of ambient RNA
753 detected. The overall summary of data quality for each sample is listed in Supplementary Table 1.
754 Next, we further assessed the data at the individual nuclei level and retained high-quality nuclei
755 with the following criteria: (1) Gene expression count (nCount_RNA) is in the range of 1,000 to
756 25,000; (2) The number of detected genes (nFeature_RNA) is greater than 400; (3) The total ATAC
757 fragment count in the peak regions (atac_peak_region_fragments) is in the range of 100 to 100,000;
758 (4) The transcription start site (TSS) enrichment score for ATAC-seq is greater than 1; (5) The
759 strength of nucleosome signal (the ratio of mononucleosome to nucleosome-free fragments) is
760 below 2. To ensure only single nuclei were analyzed, we measured the doublet probability by
761 Scrublet[81] and excluded all potential doublets receiving a score greater than 0.3 for downstream
762 analyses. In total, 243,535 nuclei that passed all QC criteria were included for further analysis.

763

## snMultiome data integration, dimensionality reduction, clustering, and cell type identification

765 For ATAC data of snMultiome analysis, open chromatin region peaks were called on individual
766 samples using MACS2 (v2.2.7)[82]. Peaks from all samples were unified into genomic intervals,
767 and the intervals falling in the ENCODE blacklisted regions were excluded[83]. Among all 398,512
768 processed ATAC peaks, top 20% of consensus peaks (n = 82,505) across all nuclei were selected
769 as variable features for downstream fragment counting and data integration. The peak-by-nuclei
770 counts for each sample were integrated by reciprocal LSI projection functions using the R
771 package Signac (v1.10.0)[84]. For RNA-seq data, normalization, data scaling and, variable features
772 detection were performed using SCTransform v2[85] in Seurat v4[18]. The cell cycle difference
773 between the G2M and S phase for each nucleus was scored and regressed out before data
774 integration. The transformed gene-by-nuclei data matrices for all nuclei passing quality control
775 were integrated by reciprocal PCA projections between different samples using Seurat v4
776 following the best practice described in Stuart et al.[84] and Butler et al.[86].

777 Weighted nearest neighbor analysis was done using Seurat v4 with 1–50 PCA components and
778 2–40 LSI components. The resulting nearest neighbor graph was used to perform UMAP
779 embedding and clustering using the SLM algorithm[87]. Clusters with known markers expressed in
780 the striatum (*ISL1* and *SIX3*) and diencephalon (*OTX2* and *GBX2*) were discarded. In addition,
781 clusters with both transcripts present in neurites (*NRGN*) and oligodendrocyte processes (*MBP*),
782 likely due to debris contamination, were discarded. These filtering steps resulted in 232,328
783 nuclei in the final dataset (Extended Data Fig. 1, Supplementary Table 2). Weighted nearest
784 neighbor, dimension reduction, and clustering were re-calculated using the filtered data. Cell
785 identities were determined based on the expression of known marker genes, as is shown in
786 Extended Data Fig. 3 and Supplementary Table 3. The 5 identified classes were progenitor,
787 neuron, glia, immune cell, and vascular cell. The 11 identified subclasses were radial glia,

24

788  intermediate progenitor cell for excitatory neurons (IPC-EN), glutamatergic neuron, GABAergic
789  neuron, intermediate progenitor cell for glia (IPC-Glia), astrocyte, oligodendrocyte precursor cell
790  (OPC), oligodendrocyte, Cajal-Retzius cell, microglia, and vascular cell. The 33 identified cell
791  types were ventricular radial glia (RG-vRG), truncated radial glia (RG-tRG), outer radial glia
792  (RG-oRG), intermediate progenitor cell for excitatory neurons (IPC-EN), newborn excitatory
793  neuron (EN-Newborn), immature intratelencephalic neuron (EN-IT-Immature), layer 2–3
794  intratelencephalic neuron (EN-L2_3-IT), layer 4 intratelencephalic neuron (EN-L4-IT), layer 5
795  intratelencephalic neuron (EN-L5-IT), layer 6 intratelencephalic neuron (EN-L6-IT), immature
796  non-intratelencephalic neuron (EN-Non-IT-Immature), layer 5 extratelencephalic neuron (EN-
797  L5-ET), layer 5–6 near-projecting neuron (EN-L5_6-NP), layer 6 corticothalamic neuron (EN-
798  L6-CT), layer 6b neuron (EN-L6b), immature dorsal lateral ganglionic eminence inhibitory
799  neuron (IN-dLGE-Immature), immature caudal ganglionic eminence inhibitory neuron (IN-
800  CGE-Immature), VIP inhibitory neuron (IN-CGE-VIP), SNCG inhibitory neuron (IN-CGE-
801  SNCG), LAMP5 inhibitory neuron (IN-CGE-LAMP5), immature medial ganglionic eminence
802  inhibitory neuron (IN-MGE-Immature), SST inhibitory neuron (IN-MGE-SST), PVALB
803  inhibitory neuron (IN-MGE-PV), intermediate progenitor cell for glia (IPC-Glia), immature
804  astrocyte (Astrocyte-Immature), protoplasmic astrocyte (Astrocyte-Protoplasmic), fibrous
805  astrocyte (Astrocyte-Fibrous), oligodendrocyte precursor cell (OPC), immature oligodendrocyte
806  (Oligodendrocyte-Immature), oligodendrocyte (Oligodendrocyte), Cajal-Retzius cell, microglia
807  (Microglia), and vascular cell (Vascular).

808

809  Cell type proportion analysis

810  The investigation of variations in cell type proportions across different age groups and brain
811  regions was conducted using a linear model approach implemented in the R packages speckle
812  (v1.2.0)[88] and limma (v3.58.1)[89]. To determine changes in cell type proportions over time, we
813  logit-transformed the proportions within each sample and fitted a linear model (~ log2_age +
814  region) using limma. Moreover, to address the potential correlation among samples from the
815  same individual, the duplicateCorrelation function in limma was applied. Once the model was fit,
816  moderated t-test with empirical Bayes shrinkage was used to test statistical significance of the
817  log2_age coefficient for each cell type. To determine cell type proportion differences between
818  PFC and V1, similar analysis was done but only samples in the third trimester and older were
819  used. Cell types with Benjamini–Hochberg adjusted P-values < 0.05 were determined significant
820  (Supplementary Table 3).

821

822  Transcription factor motif enrichment analysis

823  The per-cell regulatory activities of transcription factors (TFs) were quantified by chromVAR
824  (v1.16.0)[90]. In brief, peaks were combined by removing any peaks overlapping with a peak with
825  a greater signal, and only peaks with a width greater than 75bp were retained for motif
826  enrichment analysis. We computed the per-cell enrichment of curated motifs from JASPAR2020
827  database[91]. In total, 633 unique human transcriptional factors were assigned to their most
828  representative motifs. The per-cell-type transcriptional activity of each TF was represented by
829  averaging the per-cell chromVAR scores within the cell type, and the cell-type-specific TFs were
830  chosen for further analysis and visualization (Supplementary Table 4).

831

## Spatial transcriptomic analysis using Multiplexed Error-Robust Fluorescence in situ Hybridization (MERFISH)

834 Spatial transcriptomic analysis using MERFISH was done using the Vizgen MERSCOPE
835 platform. We designed a customized 300-gene panel composed of cell type markers
836 (Supplementary Table 5b) using online tools at https://portal.vizgen.com/. Fresh frozen human
837 brain tissue samples were sectioned at a thickness of 10 μm using a cryostat and mounted onto
838 MERSCOPE slides (Vizgen). Sections were fixed with 4% formaldehyde, washed three times
839 with PBS, photo-bleached for 3 h, and stored in 70% ethanol for up to one week. Hybridizations
840 with gene probes were performed at 37°C for 36–48 h. Next, sections were fixed using
841 formaldehyde and embedded in a polyacrylamide gel. After gel embedding, tissue samples were
842 cleared using a clearing mix solution supplemented with proteinase K for 1–7 days at 37°C until
843 no visible tissue was evident in the gel. Next, sections were stained for DAPI and PolyT and
844 fixed with formaldehyde before imaging. The imaging process was done on the MERSCOPE
845 platform according to the manufacturer's instructions. Cell segmentation was done using the
846 Watershed algorithm based on Seed Stain (DAPI) and Watershed Stain (PolyT).

847

## MERFISH data integration, dimensionality reduction, clustering, cell type assignment, and niche analysis

850 Standard MERSCOPE output data were imported into Seurat v5[92]. We retained high-quality cells
851 with the following criteria: (1) Cell volume is greater than 10 $\mu m^3$; (2) Gene expression count
852 (nCount_Vizgen) is in the range of 25 to 2,000; (3) The number of detected genes (nFeature_
853 Vizgen) is greater than 10. Normalization, data scaling and variable features detection were
854 performed using SCTransform v2[85]. The transformed gene-by-cell data matrices for all cells
855 passing quality control were integrated by reciprocal PCA projections between samples using 1–
856 30 PCA components. After integration, nearest neighbor analysis was done with 1–30 PCA
857 components. The resulting nearest neighbor graph was used to perform UMAP embedding and
858 clustering using the Louvain algorithm[93]. Clusters with markers known to be mutually exclusive
859 were deemed doublets and discarded. These filtering steps resulted in 404,030 cells in the final
860 dataset (Supplementary Table 6). The identity of specific cell types was determined based on the
861 expression of known marker genes, as is shown in Extended Data Fig. 4b. Niches were identified
862 by k-means clustering cells based on the identities of their 50 nearest spatial neighbors.

863

## Neighborhood enrichment and intercellular communication modeling

865 To evaluate the spatial proximity of cell types in each sample, we obtained a neighborhood
866 enrichment z-score using the nhood_enrichment function from Squidpy (v1.2.3)[94]. The graph
867 neural network-based node-centric expression modeling (NCEM v0.1.4) method[28] was used for
868 intercellular communication modeling (Supplementary Table 7). A node-centric linear expression
869 analysis was implemented to predict gene expression states from both cell type annotations and
870 the surrounding neighborhood of each cell, where dependencies between sender and receiver cell
871 types were constrained by the connectivity graph with a mean number of neighbors around 10
872 for each cell within each sample. One exception is that sample ARKFrozen-65-V1 was randomly
873 downsampled to 60,000 cells to ensure it has a similar neighborhood size to other samples.

874 Significant interactions were called if the magnitude of interactions (the Euclidean norm of
875 coefficients in the node-centric linear expression interaction model) was above 0.5 and at least 25
876 differentially expressed genes (q value < 0.05 for specific sender-receiver interaction terms) were
877 detected. For visualization purposes, only significant interactions were plotted in circular plots.

878

879 Quantification of ligand-receptor (LR) communication using CellChat

880 We implemented CellChat (v1.6.1)[29] to quantify the strength of interactions among cell types
881 using default parameter settings (Supplementary Table 8). After normalization, the batch-
882 corrected gene expression data from all 232,328 nuclei were taken as the CellChat input. We
883 considered all curated ligand-receptor pairs from CellChatDB, where higher expression of
884 ligands or receptors in each cell type was identified to compute the probability of cell-type-
885 specific communication at the LR pair level (refer to the original publication for details). We
886 filtered out the cell-cell communication if less than ten cells in the outgoing or incoming cell
887 types expressing the ligand or receptor, respectively. The computed communication network was
888 then summarized at a signaling pathway level and was aggregated into a weighted-directed graph
889 by summarizing the communication probability. The calculated weights represent the total
890 interaction strength between any two cell types. The statistically significant LR communication
891 between the two groups were determined by permutation test, where P value < 0.05 is considered
892 significant.

893

894 Gene regulatory network analysis

895 We implemented the SCENIC+ (v0.1.dev448+g2c0bafd) workflow[30] to build gene regulatory
896 networks of developing human neocortex based on the snMultiome data. As running the
897 workflow on all nuclei is memory intensive, we subsampled 10,000 representative nuclei by
898 geometric sketching[95] to accelerate the analyses while preserving rare cell states and the overall
899 data structure. First, MACS2 was used for consensus peak calling in each cell type[82]. Each peak
900 was extended for 250bp in both directions from the summit. Next, weak peaks were removed,
901 and the remaining peaks were summarized into a peak-by-nuclei matrix. Topic modeling was
902 performed on the matrix by pycisTopic[96] using default parameters, and the optimal number of
903 topics (48) was determined based on log-likelihood metrics. Three different methods were used
904 in parallel to identify candidate enhancer regions: (1) Regions of interest were selected by
905 binarizing the topics using the Otsu method; (2) Regions of interest were selected by taking the
906 top 3,000 regions per topic; (3) Regions of interest were selected by calling differentially
907 accessible peaks on the imputed matrix using a Wilcoxon rank sum test (logFC > 0.5 and
908 Benjamini–Hochberg adjusted P values < 0.05). Pycistarget and discrete element method
909 (DEM) based motif enrichment analysis were then implemented to determine if the candidate
910 enhancers were linked to a given TF[97]. Next, eRegulons, defined as TF-region-gene triplets
911 consisting of a specific TF, all regions that are enriched for the TF-annotated motif, and all genes
912 linked to these regions, were determined by a wrapper function provided by SCENIC+ using the
913 default settings. We applied a standard eRegulon filtering procedure: (1) Only eRegulons with
914 more than ten target genes and positive region-gene relationships were retained; (2) Only genes
915 with top TF-to-gene importance scores were selected as the target genes for each eRegulon; 3)
916 eRegulons with an extended annotation was only kept if no direct annotation is available. After
917 filtering, 582 eRegulons were retained (Supplementary Table 9). For each retained eRegulon,

27

918 specificity scores were calculated using the RSS algorithm based on region- or gene-based
919 eRegulon enrichment scores (AUC scores)[98] (Supplementary Table 10). eRegulons with top
920 specificity scores in each cell type were selected for visualization. Finally, we extended our
921 eRegulon enrichment analysis from the 10,000 sketched nuclei to all 232,328 nuclei by
922 computing the gene-based AUC scores for all 582 eRegulons using the R package AUCell
923 (v1.20.2)[31] with default settings.

924

925 <u>Trajectory inference and trajectory-based differential expression analysis</u>

926 Cells belonging to excitatory neuronal lineages, including radial glial cells, IPC-EN, and
927 glutamatergic neurons, were selected from the whole dataset for trajectory inference using
928 Slingshot (v2.6.0)[32]. Weighted nearest neighbor graph was re-calculated on the subset using 1–50
929 PCA components and 2–40 LSI components. Dimension reduction was performed based on the
930 calculated nearest neighbor graph, generating an 8-dimensional UMAP embedding. We
931 identified 23 clusters in this UMAP space after removing one outlier cluster using mclust[99] .
932 Next, we identified the global lineage structure with a cluster-based minimum spanning tree
933 (MST). The cluster containing RG-vRG was set as the starting cluster, and those containing
934 terminally differentiated cells were set as ending clusters (Extended Data Fig. 8a). Subsequently,
935 we fitted nine simultaneous principal curves to describe each of the nine lineages, obtaining each
936 cell's weight based on its projection distance to the curve representing that lineage. Pseudotimes
937 were inferred based on the principal curves, and shrinkage was performed for each branch for
938 better convergence (Supplementary Table 11). Finally, the principal curves in the 8-dimensional
939 UMAP space were projected to a 2-dimensional UMAP space for visualization.

940

941 <u>Identification of eRegulon modules</u>

942 To model the activity of eRegulons along inferred trajectories, we fitted gene-based eRegulon
943 AUC scores against pseudotimes by a generalized additive model (GAM) using tradeSeq
944 (v1.12.0)[33]. As AUC scores can be seen as proportions data on (0,1), instead of the default
945 negative binomial GAM, we fitted a beta GAM with six knots in tradeSeq. Fitted values from the
946 tradeSeq models were extracted using the predictSmooth function, with 100 data points along
947 each trajectory. The oRG&tRG trajectory was removed because we focused on excitatory
948 neuronal lineages for eRegulon analysis. Based on fitted AUC values, six eRegulon modules
949 were identified by k-means clustering (Supplementary Table 12a).

950

951 <u>Gene ontology enrichment analysis for eRegulon modules</u>

952 The one-sided hypergeometric test implemented in clusterProfiler v4.0.5[100] was used to identify
953 overrepresented gene ontology (biological pathway) in each eRegulon module (Supplementary
954 Table 12b). Genes present in at least 8% of all eRegulons in a module were regarded as the core
955 target genes of that module. Module-specific core target gene sets were used as input gene sets.
956 The union of target genes of any eRegulon was used as the background.

957

958 <u>Differential gene expression analysis between common and V1-specific EN-L4-IT</u>

959  To identify genes differentially expressed between common and V1-specific EN-L4-IT, we first
960  selected all EN-L4-IT nuclei and determined their subtype identity (common or V1-specific)
961  based on markers and tissue of origin (Extended Data Fig. 9a,b). We then aggregated counts
962  across samples and subtypes to generate pseudobulk samples. Differential gene expression
963  analysis was done by fitting the pseudobulked count data to a generalized linear mixed model (~
964  subtype + log2_age + [1 | dataset]) using the R package glmmSeq (v0.5.5)[101]. Size factors and
965  dispersion were estimated using the R package edgeR (v3.42.4)[102]. Once the model was fit,
966  likelihood ratio tests were used to determine statistical significance using (~log2_age + [1 |
967  dataset]) as the reduced model. Genes with Benjamini–Hochberg adjusted P-values < 0.05 were
968  determined significant (Supplementary Table 13).

969

970  Identification of key eRegulons that regulate neuronal lineage divergence

971  Based on the principal curves, five bifurcation points (BPs) were identified along neuronal
972  differentiation. To identify genes that are differentiating around a BP of the trajectory, we
973  performed an earlyDETest using tradeSeq. Specifically, we first separated the pseudotimes into
974  five consecutive segments (Extended Data Fig. 8g). We then compared the expression patterns of
975  gene-based eRegulon AUCs along pseudotime between lineages by contrasting 12 equally
976  spaced pseudotimes within segments that enclose the BP (Supplementary Table 14). We included
977  segments 2–3 for BP1, segments 3–4 for BP2, and segments 4–5 for BP3, BP4, and BP5.

978

979  Isolation and in vitro culture of glial progenitors from late second-trimester human cortex

980  Glial progenitor cells were isolated from GW20–24 human dorsal cortical tissue samples. The
981  ventricular zone/inner subventricular zone (VZ/iSVZ) and outer subventricular zone (oSVZ)
982  were dissected and dissociated using the Papain Dissociation System (Worthington
983  Biochemical). Dissociated cells were layered onto undiluted papain inhibitor solution
984  (Worthington Biochemical) and spun down at $70 \times g$ for 6 min to eliminate debris. The cell pellet
985  was resuspended in 10 mL complete culture medium (DMEM/F12, 2 mM GlutaMAX, 2% B27
986  without vitamin A, 1% N2, and $1 \times$ Penicillin-Streptomycin) and incubated at 37°C for 3 h for
987  surface antigen recovery. From this point on, cells were handled on ice or at 4°C. Cells were
988  washed once with staining buffer (Hank's Balanced Salt Solution [HBSS] without $Ca^{2+}$ and
989  $Mg^{2+}$, 10 mM HEPES pH 7.4, 1% BSA, 1 mM EDTA, 2% B27 without vitamin A, 1% N2, and 1
990  $\times$ Penicillin-Streptomycin), spun down at $300 \times g$ for 5 min, and resuspended in staining buffer
991  to a density of $1 \times 10^8$ cells/mL. Cells were blocked by FcR Blocking Reagent (Miltenyi
992  Biotech, 1:20) for 10 min, followed by antibody incubation for 30 min. Antibodies used for
993  FACS include FITC anti-EGFR (Abcam, ab11400), PE anti-F3 (Biolegend, 365204), PerCP-
994  Cy5.5 anti-CD38 (BD Biosciences, 551400), Alexa Fluor 647 anti-PDGFRA (BD Biosciences,
995  562798), and PE-Cy7 anti-ITGA2 (Biolegend, 359314). All antibodies were used at 1:20
996  dilution. After incubation, cells were washed twice in staining buffer, resuspending in staining
997  buffer containing Sytox Blue (Invitrogen), and sorted using BD FACSAria II sorters. Cells were
998  sorted into collection buffer (HBSS without $Ca^{2+}$ and $Mg^{2+}$, 10 mM HEPES pH 7.4, 5% BSA,
999  2% B27 without vitamin A, 1% N2, and $1 \times$ Penicillin-Streptomycin). After sorting, cells were
1000 spun down at $300 \times g$ for 5 min, resuspended in complete culture medium, and plated onto glass
1001 coverslips pre-coated with poly-D-lysine and laminin at a density of $2.5 \times 10^4$ cells/cm². Cells

1002 were cultured in a humidified incubator with 5% $CO_2$ and 8% $O_2$. Half of the medium was
1003 changed with fresh medium every 3–4 days until harvest at the indicated time.
1004

1005 <u>Immunostaining and confocal imaging</u>

1006 On DIV0 and DIV14, glial progenitors or their progenies were fixed with 4% formaldehyde/4%
1007 sucrose in PBS and permeabilized/blocked with PBS-based blocking buffer containing 10%
1008 donkey serum, 0.2% gelatin, and 0.1% Triton X-100 at room temperature for 1 h. Samples were
1009 then incubated with primary antibodies diluted in the blocking buffer at 4 °C overnight. The next
1010 day, samples were washed in PBS three times and incubated with secondary antibodies in the
1011 blocking buffer at room temperature for 1 h. Samples were then washed twice in PBS,
1012 counterstained with DAPI, and washed in PBS again. Z-stack images were acquired with a Leica
1013 TCS SP8 using a 25× water immersion objective. Acquired images were processed using Imaris
1014 v9.7 (Oxford Instruments) and Fiji/ImageJ v1.54 [103]. The following antibodies were used: TFAP2C
1015 (R&D systems, AF5059, 1:50), CRYAB (Abcam, ab13496, 1:200), NeuN (EMD Millipore,
1016 ABN90, 1:250), OLIG2 (Abcam, ab109186, 1:150), EGFR (abcam, ab231, 1:200), SPARCL1
1017 (R&D systems, AF2728, 1:50), and DLX5 (Sigma, HPA005670, 1:100).

1018

1019 <u>Single-cell RNA-seq analysis of glial progenitor differentiation</u>

1020 Glial progenitors were either immediately subjected to single-cell RNA-seq or cultured in vitro
1021 for 7 and 14 days before single-cell RNA-seq. In the latter cases, cells were released using the
1022 Papain Dissociation System (Worthington Biochemical) without DNase for 20 min. Released
1023 cells were washed twice in HBSS without $Ca^{2+}$ and $Mg^{2+}$ supplemented with 0.04% BSA, spun
1024 down at 250 × g for 5 min, and resuspended in HBSS without $Ca^{2+}$ and $Mg^{2+}$ supplemented with
1025 0.04% BSA. Cells were counted using a hemocytometer, diluted to ~1000 nuclei/μL, and further
1026 processed following the 10X Genomics Chromium Single Cell 3' Reagent Kits User Guide (v3.1
1027 Chemistry). We targeted 10,000 cells per sample per reaction. Libraries from individual samples
1028 were pooled and sequenced on the NovaSeq 6000 sequencing system, targeting 22,500 read pairs
1029 per cell.

1030 The raw sequencing signals in the BCL format were demultiplexed into fastq format using the
1031 "mkfastq" function in the Cell Ranger suite (v.7.1.0, 10x Genomics). Cell Ranger count pipeline
1032 was implemented for cell barcode calling, reads alignment, and quality assessment using the
1033 human reference genome (GRCh38) following the protocols described by 10X Genomics. The
1034 pipeline assessed the overall quality to retain all intact cells from the background and filtered out
1035 non-cell associated reads. All gene expression libraries in this study showed a high fraction of
1036 reads in cells, indicating high RNA content in called cells and minimal levels of ambient RNA
1037 detected. The overall summary of data quality for each sample is listed in Supplementary Table
1038 15. Next, we further assessed the data at the individual cell level and retained high-quality cells
1039 with the following criteria: (1) The number of detected genes (nFeature_RNA) is greater than
1040 1000 and less than 10,000; (2) less than 10% of all reads mapped to mitochondrial genes. Raw
1041 counts were log-normalized with a size factor of 10,000. The first 30 principal components were
1042 used to construct the nearest neighbor graph and Louvain clustering was used to identify clusters.
1043 Clusters with significantly fewer UMI counts, likely consisting of low-quality, dying cells, were
1044 also excluded for further analysis. The identity of specific cell types was determined based on the
1045 expression of known marker genes (Extended Data Fig. 11k, Supplementary Table 16). The 10

1046 identified cell types were dividing cell (Dividing), radial glia (RG), ependymal cell (Ependymal
1047 cell), intermediate progenitor cell for excitatory neurons (IPC-EN), tripotential intermediate
1048 progenitor cell (Tri-IPC), astrocyte (Astrocyte), oligodendrocyte precursor cell (OPC),
1049 intermediate progenitor cell for inhibitory neurons (IPC-IN), and inhibitory neurons (IN).

1050

1051 ## Clonal analysis of glial progenitors

1052 For clonal analysis, samples for FACS were processed as above with the following changes:
1053 individual tRG, oRG, or Tri-IPC was sorted using a BigFoot Spectral Cell Sorter (Thermo Fisher)
1054 via single-cell precision mode into a single well of 96-well glass-bottom plates pre-coated with
1055 polyethylenimine and laminin containing 100 μL complete culture medium. For tRG and oRG, the
1056 complete culture medium was supplemented with 10 ng/mL FGF2 to promote initial cell survival
1057 and proliferation. The culture medium was changed weekly for a total of two weeks. After two
1058 weeks, cells were fixed and stained in the same way as mentioned above. The following antibodies
1059 were used: EOMES (Abcam, ab23345, 1:200), OLIG2 (EMD Millipore, MABN50, 1:200), EGFR
1060 (abcam, ab231, 1:200), SPARCL1 (R&D systems, AF2728, 1:50), SOX10 (Santa Cruz, sc-365692,
1061 1:50) and DLX5 (Sigma, HPA005670, 1:100).

1062

1063 ## Glial progenitor slice transplantation assay

1064 Primary cortical tissue from GW 20-24 was maintained in artificial cerebrospinal fluid (ACSF)
1065 containing 110 mM Choline chloride, 2.5 mM KCl, 7 mM $MgCl_2$, 0.5 mM $CaCl_2$, 1.3 mM
1066 $NaH_2PO_4$, 25 mM $NaHCO_3$, 10 mM D-(+)-glucose, and 1 × Penicillin-Streptomycin. Before use,
1067 ACSF was bubbled with 95% O2/5% CO2. Cortical tissue was embedded in a 3.5% low melting
1068 agarose gel. Embedded tissue was acutely sectioned at 300 μm using a vibratome (Leica) before
1069 being plated on Millicell inserts (Millipore, PICM03050) in 6 well tissue culture plates. Tissue
1070 slices were cultured at the air-liquid interface in media containing 32% HBSS, 60% Basal
1071 Medium Eagle, 5% FBS, 1% glucose, 1% N2 and 1 × Penicillin-Streptomycin-Glutamine. Slices
1072 were maintained for 8 days in culture at 37°C and the medium was changed every other day.

1073 Glial progenitors were isolated by FACS, as mentioned above. About 200,000 Cells were spun
1074 down at 300 × g for 5 min and resuspended in 0.5 mL complete culture medium containing 1 ×
1075 $10^7$ PFU CMV-GFP adenoviruses (Vector Biolabs). Next, cells were incubated in a low
1076 attachment plate for 1 hour under the normal culture condition. After infection, cells were
1077 washed twice with complete culture medium containing 0.3% BSA and resuspended in slice
1078 culture medium. About 25,000 cells were transplanted onto the oSVZ of freshly prepared slices
1079 through a pipette.

1080 After 8 days in culture, slices were fixed with 4% formaldehyde in PBS at room temperature for
1081 1 h, followed by permeabilization and blocking with PBS-based blocking buffer containing 10%
1082 donkey serum, 0.2% gelatin, and 1% Triton X-100 at room temperature for 1 h. Samples were
1083 then incubated with primary antibodies diluted in the blocking buffer at 4 °C for 48 h. Two days
1084 later, samples were washed in PBS plus 0.1% Triton X-100 four times and incubated with
1085 secondary antibodies in the blocking buffer at 4 °C for 24 h. After secondary antibody
1086 incubation, samples were washed twice in PBS plus 0.1% Triton X-100, counterstained with
1087 DAPI, and washed in PBS again. Z-stack images were acquired with a Leica TCS SP8 using a
1088 25× water immersion objective. Acquired images were processed using Imaris v9.7 (Oxford

1089   Instruments) and Fiji/ImageJ v1.54 [103]. The following antibodies were used: GFP (Aveslabs,
1090   GFP-1020, 1:1,000), EOMES (Abcam, ab23345, 1:200), NeuN (EMD Millipore, ABN90,
1091   1:250), OLIG2 (EMD Millipore, MABN50, 1:200), EGFR (Abcam, ab32077, 1:200), DLX5
1092   (Sigma, HPA005670, 1:100), and SPARCL1 (R&D systems, AF2728, 1:50).

1093

1094   <u>Classification of Tri-IPC-derived inhibitory neurons</u>

1095   Human ganglionic eminence single-cell RNA-seq data from Shi et al.[44] were downloaded from
1096   GEO (GSE135827) and used as the reference. We integrated all samples using the RPCA
1097   methods, subset the data to focus on cells from the ganglionic eminence, re-clustered the cells,
1098   and annotated interneuron subtypes based on marker genes reported in the literature[45] (Extended
1099   Data Fig. 13a,b).

1100   To determine the identity of Tri-IPC-derived inhibitory neurons based on the reference dataset,
1101   we applied SingleCellNet (v0.1.0), a random-forest-based cell type classification method.
1102   Specifically, we randomly selected 400 cells from each cell type as the training set. We found the
1103   top 200 most differentially expressed genes per cell type, and then ranked the top 200 gene pairs
1104   per cell type from those genes. The preprocessed training data were then transformed according
1105   to the selected gene pairs and were used to build a multi-class classifier of 1000 trees.
1106   Additionally, we created 400 randomized cell expression profiles to train up an "unknown"
1107   category in the classifier. After the classifier was built, we selected 100 cells from each cell type
1108   from the held-out data, along with another 100 randomized cells, and assessed the performance
1109   of the classifier on the held-out data using Precision-Recall curves, obtaining an average AUPRC
1110   of 0.901. To classify Tri-IPC-derived inhibitory neurons, we transformed the query data with top
1111   pairs selected from the optimized training data and classified it with the trained classifier. Here,
1112   we chose a classification score threshold of 0.35, and cells with scores below this threshold were
1113   assigned as unmapped.

1114   As an alternative classification method to determine the identity of Tri-IPC-derived inhibitory
1115   neurons, we performed mutual nearest neighbors-based label transfer using the MapQuery()
1116   function in Seurat v4. The first 30 principal components were used to identify transfer anchors.
1117   Cell type labels from Shi et al. were transferred to Tri-IPC-derived inhibitory neurons when
1118   confidence was high (prediction score > 0.5). Cells with prediction scores equal to or lower than
1119   0.5 were labeled as unmapped.

1120

1121   <u>Classification of Tri-IPC-derived astrocytes</u>

1122   Mouse single-cell RNA-seq data from Di Bella et al.[48] were downloaded from the Single Cell
1123   Portal (SCP1290) and used as the reference. We subset the data and focused on astrocytes and
1124   cycling glial cells (defined by the original authors). These cells were re-clustered and annotated
1125   as Olig2 or S100a11 lineages based on marker genes reported in the literature[47] (Extended Data
1126   Fig. 13e,f). We used Tri-IPC-derived astrocytes as the query data and applied SingleCellNet in
1127   the same way as for Tri-IPC-derived inhibitory neurons. We also applied Seurat label transfer in
1128   the same way, except that 20 principal components were used to identify transfer anchors.

1129   We also used astrocytes at the infancy stage from our snMultiome data, when we were able to
1130   distinguish the two astrocyte lineages, as the reference. We selected the astrocytes at infancy
1131   from the whole dataset and redid nearest neighbor analysis with 1–50 PCA components (already

1132   computed after SCTransform and RPCA integration). These cells were re-clustered on the basis
1133   of the resulting nearest neighbor graph and annotated on the basis of marker genes reported in
1134   the literature[47] (Extended Data Fig. 13i,j). We used Tri-IPC-derived astrocytes as the query data,
1135   which was re-processed in the same way as snMultiome data, including SCTransform v2
1136   modeling and cell cycle regression. SingleCellNet was applied in the same way as above. For
1137   Seurat label transfer, the first 50 principal components were used to identify transfer anchors.

1138

1139   <u>Building single-cell risk map for cognitive traits and brain disorders by SCAVENGE</u>

1140   We implemented SCAVENGE (v1.0.2)[51] to integrate the snATAC-seq part of the snMultiome
1141   data with GWAS data of four cognitive traits (fluid intelligence, processing speed, executive
1142   function, and working memory) and five neuropsychiatric disorders (autism spectrum disorder
1143   [ASD], major depressive disorder [MDD], bipolar disorder [BPD], attention-deficit/hyperactivity
1144   disorder [ADHD], and schizophrenia [SCZ]). Analysis of Alzheimer's disorder was included as a
1145   positive control. For each trait or condition, we performed multi-SNP-based conditional and joint
1146   association analysis on all GWAS SNPs with default settings. A stepwise model selection
1147   procedure was implemented to select independently associated SNPs and compute the fine-
1148   mapped posterior probability (PP). The PP was imported for our subsequent gchromVAR
1149   analysis[104], where we built a cell-by-peak count matrix using peak called from integrated
1150   snATAC-seq data. A gchromVAR score indicating potential GWAS signal enrichment over a set
1151   of background peaks was calculated for each cell after correcting GC bias. To minimize the batch
1152   effects, we used the batch-aligned LSI matrix for the nearest neighbor graph construction and
1153   subsequent network propagation. A trait relevant score (TRS) representing the potential GWAS
1154   risk association was assigned to each cell for constructing the single-cell risk map for cognitive
1155   traits or neurological disorders. To determine the significant trait-cell association, we considered
1156   cells receiving top the 0.1% TRS score as traits-relevant and permuted the network propagation
1157   1000 times for statistical significance. Cells with a P value less than 0.05 were defined as trait
1158   associated. To determine the trait relevance per cell type, we calculated the odds ratio of
1159   associated cells with each trait in each cell type over the background and determined statistical
1160   significance by hypergeometric test followed by Benjamini-Hochberg correction. Cell types with
1161   FDR < 0.05 and odds ratio > 1.4 were deemed significantly enriched for trait-associated variants.
1162   Similar analysis were done for regions and age groups. Finally, the TRS scores were
1163   standardized by z transformation for comparison and visualization (Supplementary Table 18,
1164   Supplementary Table 19). The GWAS data used in this study can be downloaded from the
1165   following links: fluid intelligence (phenocode 20016), processing speed (phenocode 20023),
1166   executive function (phenocode 399), and working memory (phenocode 4282):
1167   https://pan.ukbb.broadinstitute.org/downloads/; ASD:
1168   https://figshare.com/articles/dataset/asd2019/14671989; MDD:
1169   https://datashare.ed.ac.uk/handle/10283/3203; BPD:
1170   https://figshare.com/articles/dataset/bip2021_noUKBB/; ADHD:
1171   https://figshare.com/articles/dataset/adhd2022/22564390; SCZ:
1172   https://figshare.com/articles/dataset/cdg2018-bip-scz/14672019; ALZ:
1173   https://ctg.cncr.nl/software/summary_statistics.

1174

1175   **Acknowledgements:**

**Author contributions:**

1188    Conceptualization: L.W., C.W., J.L., A.R.K.; data curation: L.W., C.W.; formal analysis: L.W.,
1189    C.W., J.A.M.; funding acquisition: L.W., E.J.H., A.A.-B., X.D., J.L., A.R.K.; investigation: L.W.,
1190    S.C., S.Z., S.W., T.M., A.C.-S., Q.B., L.G.O., M.S.; methodology: L.W., S.Z., A.C.-S., X.G.;
1191    resources: S.W., M.F.P., E.J.H., A.R.K.; software: L.W., C.W., J.A.M., J.J.A., G.Z.; supervision:
1192    A.A.-B., X.D., J.L., A.R.K.; visualization: L.W., C.W., J.A.M.; writing – original draft: L.W.,
1193    C.W., J.A.M.; writing – review & editing: all authors.

**Data availability:** All raw and processed snMultiome sequencing data were deposited to NeMO
archive and will be accessible at https://assets.nemoarchive.org/dat-oiif74w. MERFISH data were
deposited to Brain Image Library. Processed data are available at an interactive portal at
https://cell.ucsf.edu/snMultiome.

**Code availability:** Code used for data analysis in this manuscript is available at GitHub
(https://github.com/complexdisease/Human_Cortex_Dev_Multiome).

**Competing interests:** A.R.K. is a co-founder, consultant, and director of Neurona Therapeutics.
The remaining authors declare no competing interests.
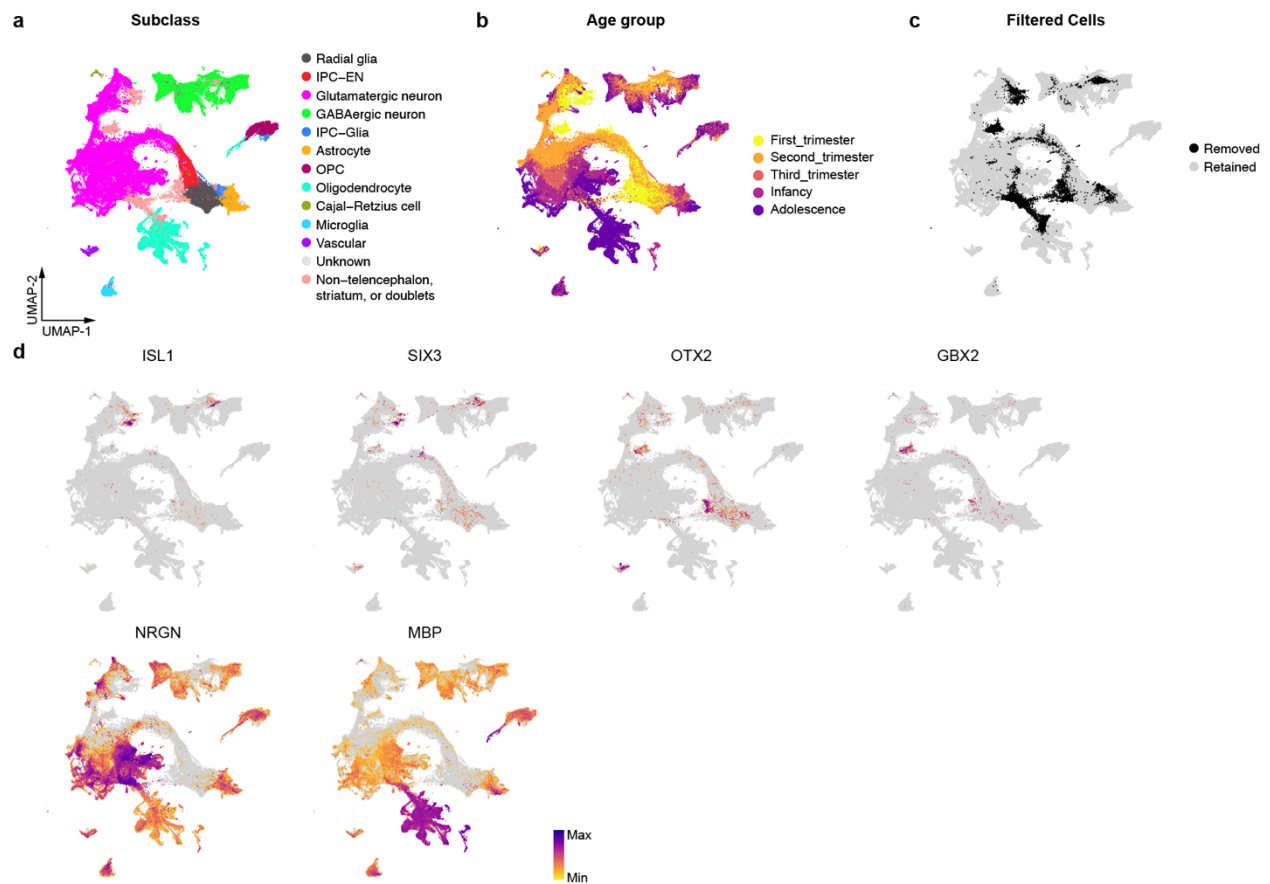
**Extended Data Fig. 1 | Filtering of the single-nucleus multiome data. a**, UMAP plots showing the distribution of cell subclasses in the single-nucleus multiome data prior to data filtering. **b**, UMAP plots showing the distribution of age groups in the single-nucleus multiome data prior to data filtering. **c**, UMAP plots showing the distribution of cells removed during data filtering. **d**, UMAP plots showing the expression levels of genes identified in the striatum (*ISL1* and *SIX3*), diencephalon (*OTX2* and *GBX2*), neuronal dendrites (*NRGN*), and oligodendrocyte processes (*MBP*).
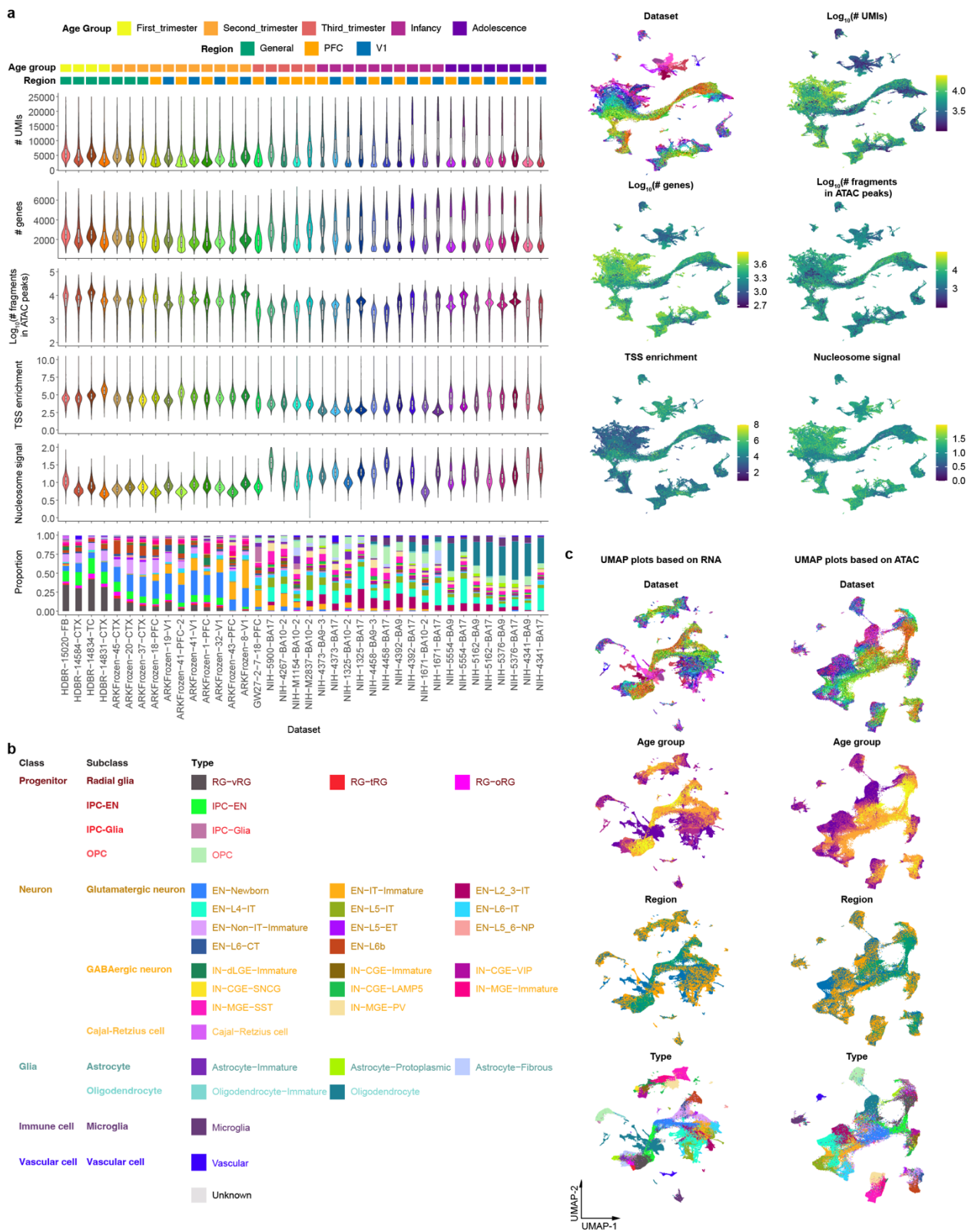
**Extended Data Fig. 2 | Quality control of the single-nucleus multiome data. a,** Violin plots, box plots, barplots, and UMAP plots of several quality control metrics for evaluating the quality of individual samples, including numbers of unique molecular identifiers (# UMIs), numbers of

1217    identified genes (# genes), number of fragments in ATAC peaks, transcription start site (TSS)
1218    enrichment scores, and proportion of individual cell types in each sample. The legend for cell types
1219    can be found in panel b. **b** Classes, subclasses, and types identified from the snMultiome data. **c**,
1220    UMAP plots generated based on RNA or ATAC data only. The legend can be found in panel a and
1221    b.

1222

1223

38
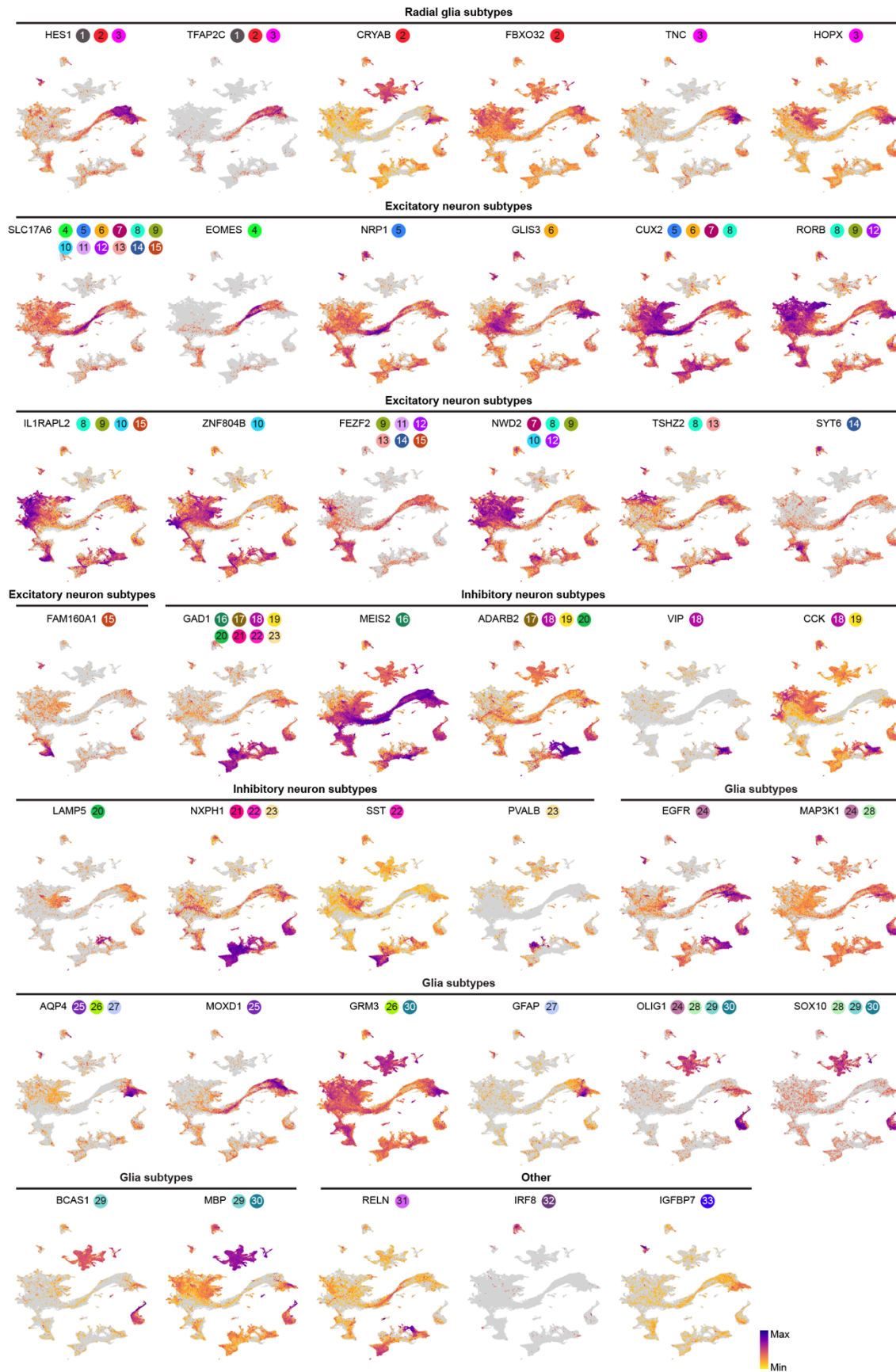
1224 **Extended Data Fig. 3 | Expression patterns of marker genes in the single-nucleus multiome**
1225 **data.** UMAP plots of all cells showing the expression levels of cell-type-specific marker genes.
1226 The colored circles and numbers pinpoint specific cell types where the gene is expressed. The
1227 legend for these numbers can be found in Fig. 1c.

1228
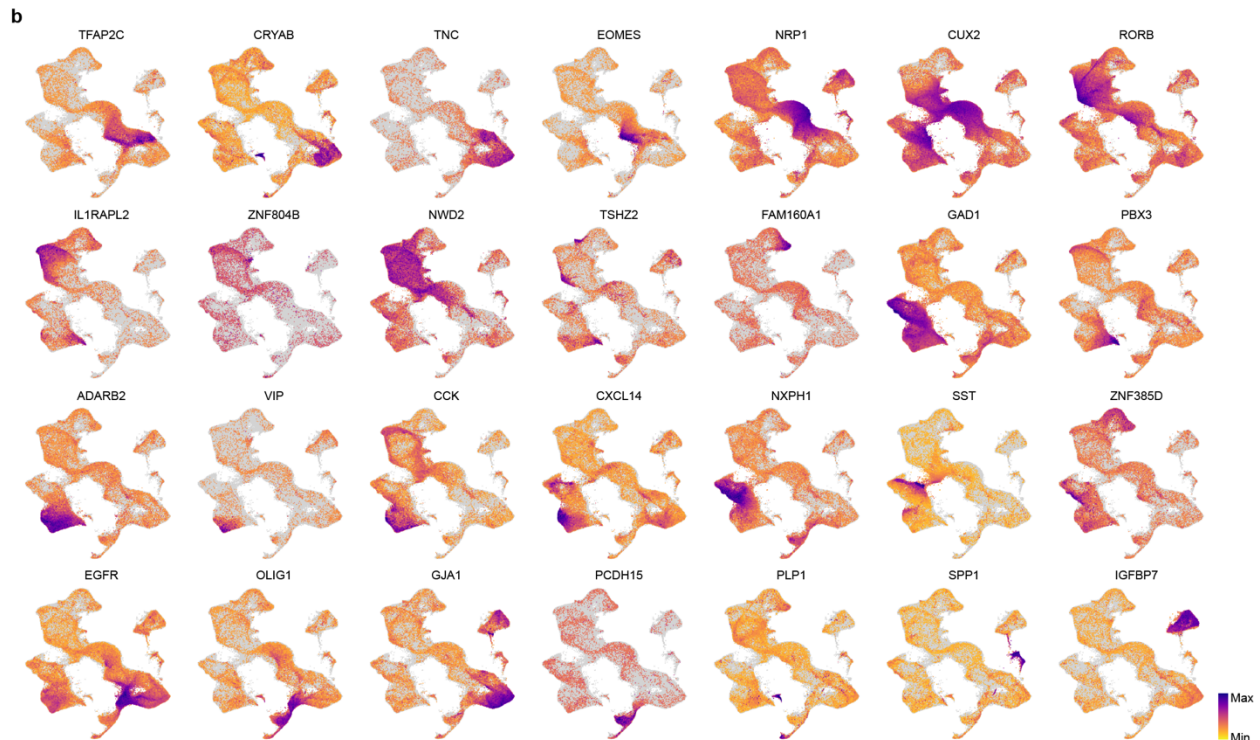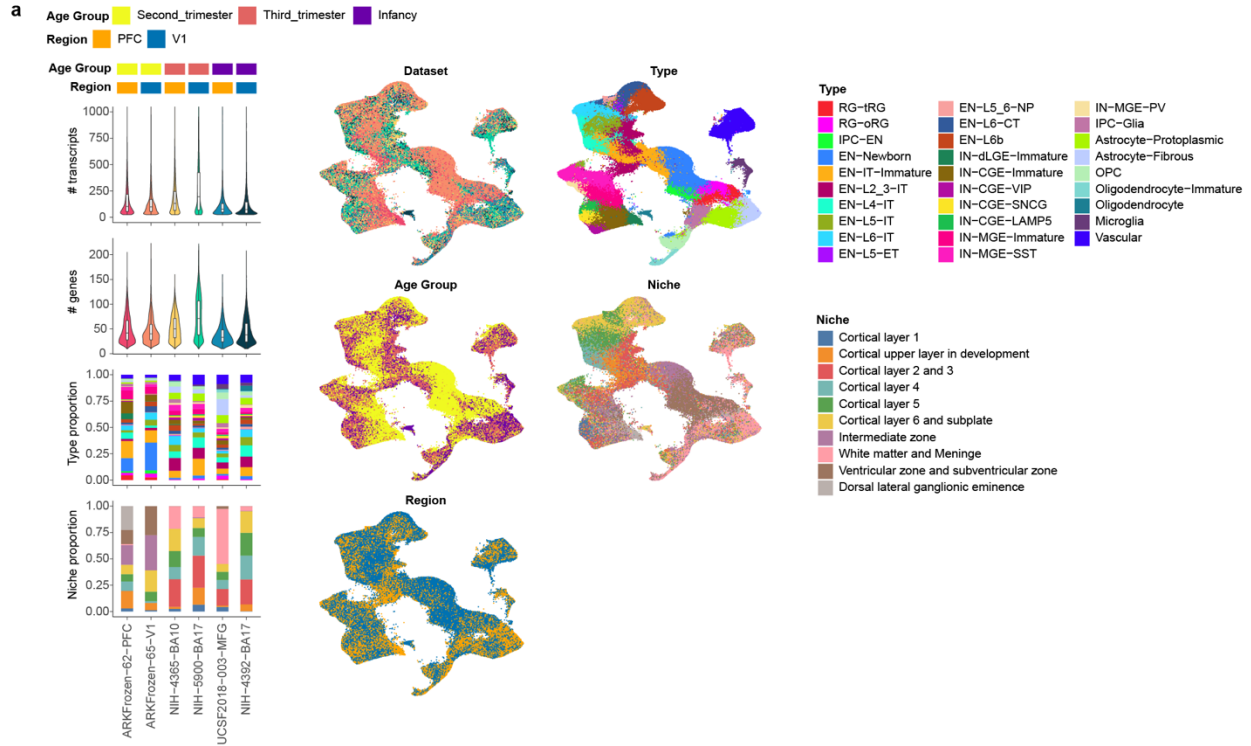
**Extended Data Fig. 4 | Quality control and annotation of MERFISH data. a,** Violin plots, box plots, barplots, and UMAP plots of several metadata of MERFISH samples, including numbers of detected transcripts (# transcript), numbers of identified genes (# genes), age groups, regions, cell

1233    types, and niches. **b**, UMAP plots of all cells in the MERFISH dataset showing the expression
1234    levels of cell-type-specific marker genes.

1235

1236

1237    **Extended Data Fig. 5 | Spatial distribution of cell types in individual MERFISH samples.**

1238

1239

44
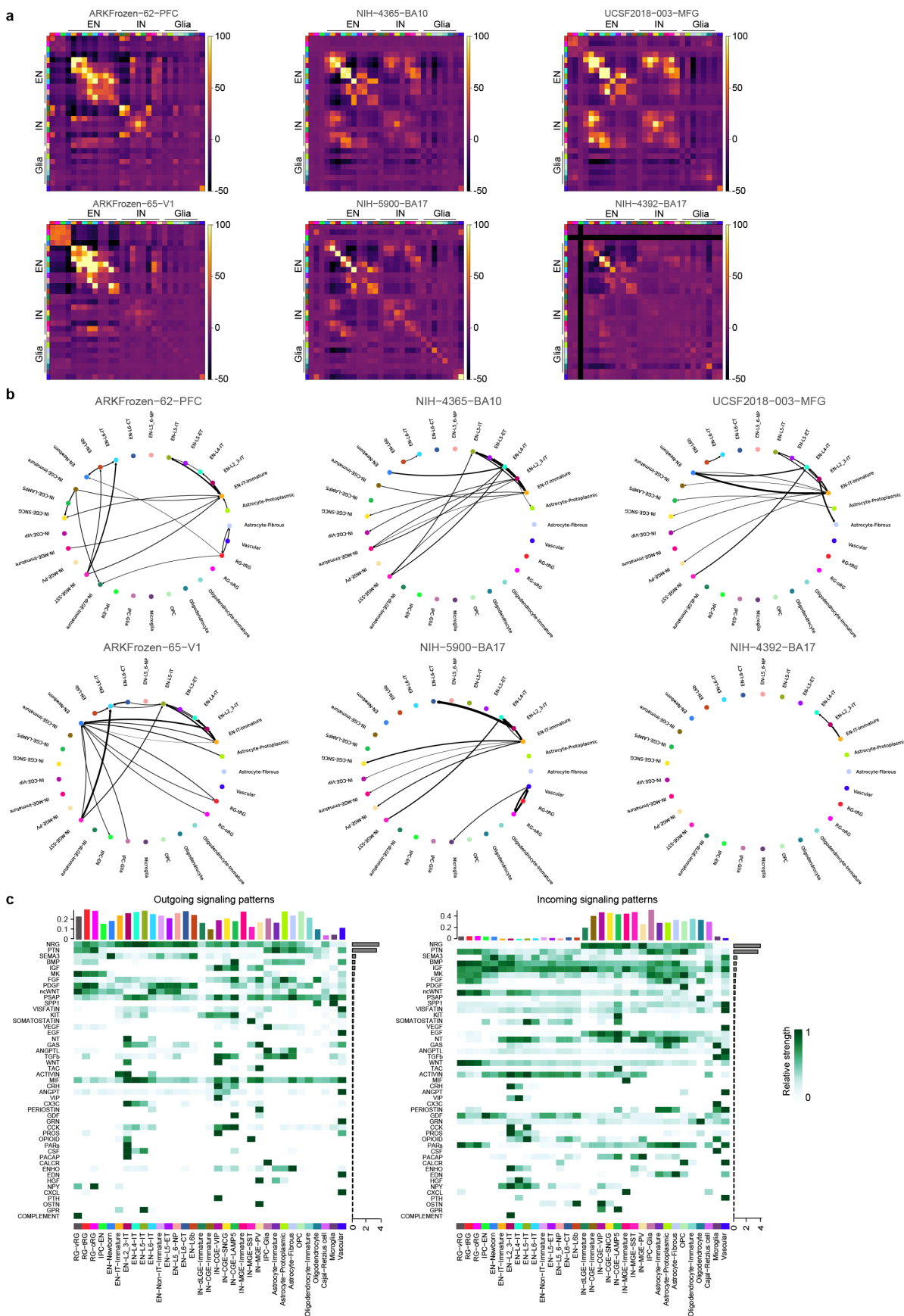
1240 **Extended Data Fig. 6 | Intercellular communication between cell types in developing human**
1241 **cortex. a**, Heatmaps showing neighborhood enrichment z scores of each MERFISH sample. The
1242 row and column annotations are color-coded by cell types, the legend of which can be found in
1243 Fig. 2a. When a particular cell type is not present in the dataset, the neighborhood enrichment z
1244 scores were arbitrarily set to $-50$. **b**, Circular maps showing significant intercellular
1245 communication determined by NCEM in each MERFISH sample. **c**, Heatmaps showing the
1246 relative strength of outgoing (left) and incoming (right) signaling pathways in individual cell types.
1247 The bar graphs on the top and right side of the heatmaps are the sum of communication probability
1248 (interaction strength) for each cell type and signaling pathway, respectively.

1249
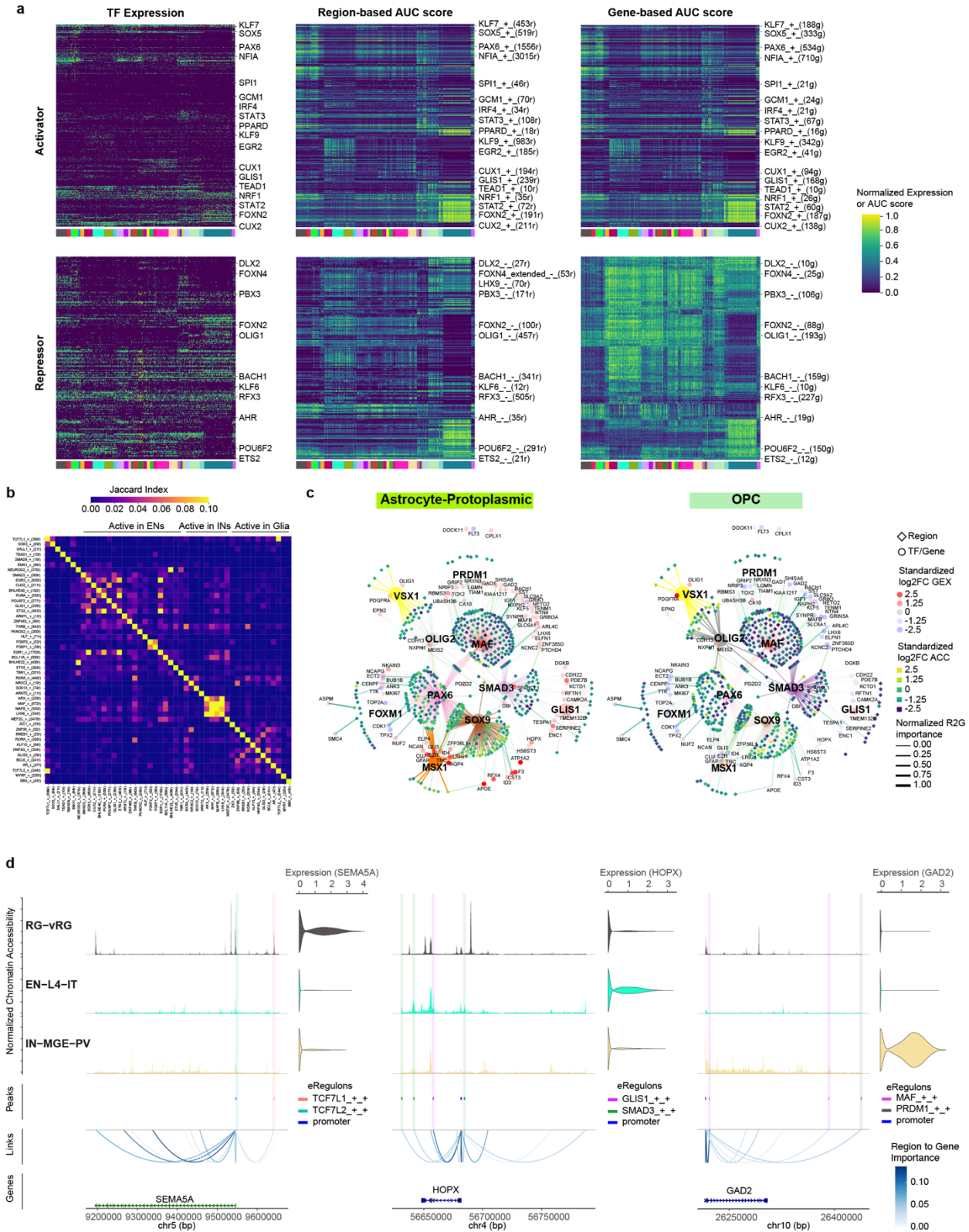
**Extended Data Fig. 7 | Cell-type-specific gene regulatory networks. a**, Heatmaps showing the min-max normalized TF expression levels, region-based AUC scores, and gene-based AUC scores of activator eRegulons across cell types. **b**, A heatmap showing Jaccard similarity matrix of target

1250

1251

1252

1253

46

1254   regions of cell-type-specific eRegulons listed in Fig. 3a. **c**, Gene regulatory networks of selective
1255   eRegulons in Astrocyte-Protoplasmics and OPCs. TF nodes and their links to enhancers are
1256   individually colored. The size and the transparency of the TF nodes represent their gene expression
1257   levels in each cell type. **d**, Coverage plots showing aggregated ATAC profiles across RG-vRGs,
1258   EN-L4-ITs, and IN-MGE-PVs on three genomic loci—*SEMA5A*, *HOPX*, and *GAD2*. Identified
1259   candidate cis-regulatory elements (cCREs) are colored by their corresponding eRegulons. Region
1260   to gene links are shown as arcs and color-scaled based on region–gene importance scores obtained
1261   from SCENIC+ analysis.

1262

1263
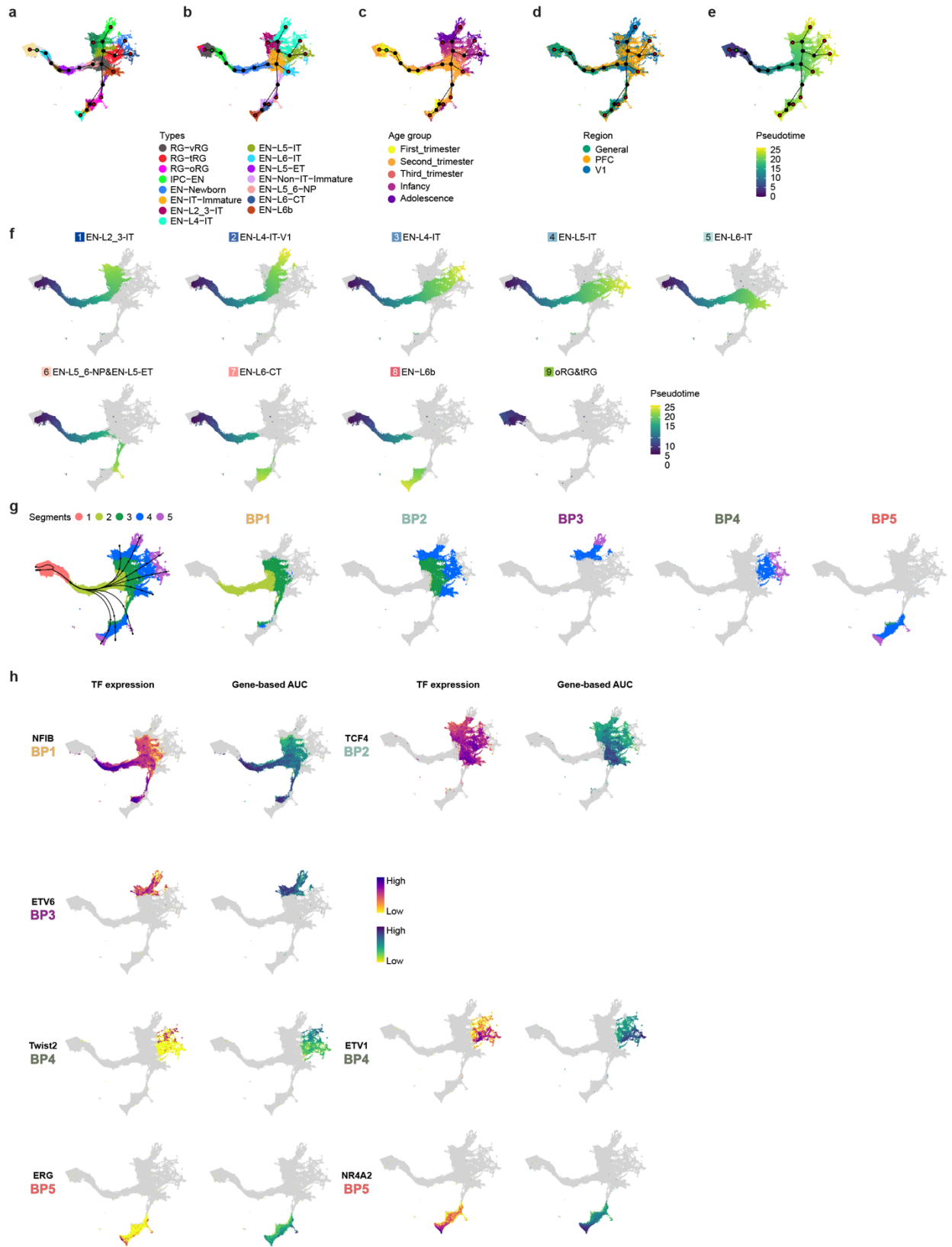
1264 **Extended Data Fig. 8 | Differentiation trajectories of excitatory neuron lineages. a–e**, UMAP
1265 plots of cells belonging to excitatory neuron lineages with clusters connected by a minimum
1266 spanning tree showing. The green node indicates the root node, and the red nodes indicate the
1267 ending nodes. Cells are color-coded by clusters (**a**), types (**b**), age groups (**c**), regions (**d**), or
1268 pseudotime (**e**). **f**, UMAP plots of each of the nine excitatory neuron lineages colored by
1269 pseudotime. **g**, UMAP plots of excitatory neuron lineages colored by the five pseudotime segments
1270 used for eRegulon activity analysis at bifurcation points. **h**, UMAP plots highlighting
1271 representative eRegulons involved in trajectory determination at bifurcation points.

1272
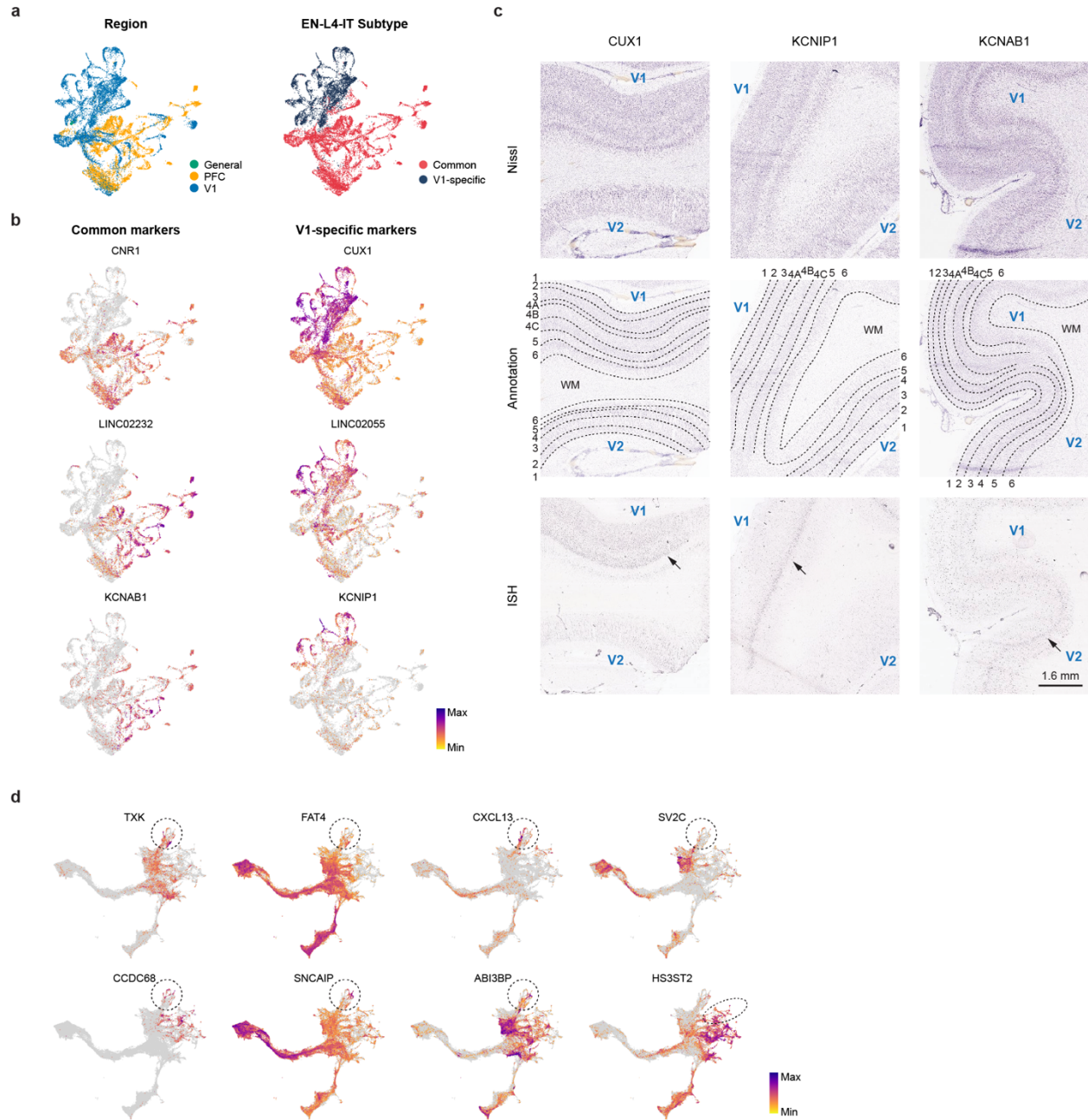
**Extended Data Fig. 9 | Markers of V1-specific EN-L4-IT subtype. a**, UMAP plots of all EN-L4-IT color-coded by regions (left) and subtypes (right). **b**, UMAP plots showing the expression levels of representative differentially expressed genes between V1-specific and common EN-L4-IT neurons. **c**, In situ hybridization (ISH) of V1-biased (*CUX1* and *KCNIP1*), and common-biased genes in EN-L4-IT neurons in adult human V1 and V2 areas. **d**, UMAP plots of EN-L4-IT subtype marker genes found in adult human V1.
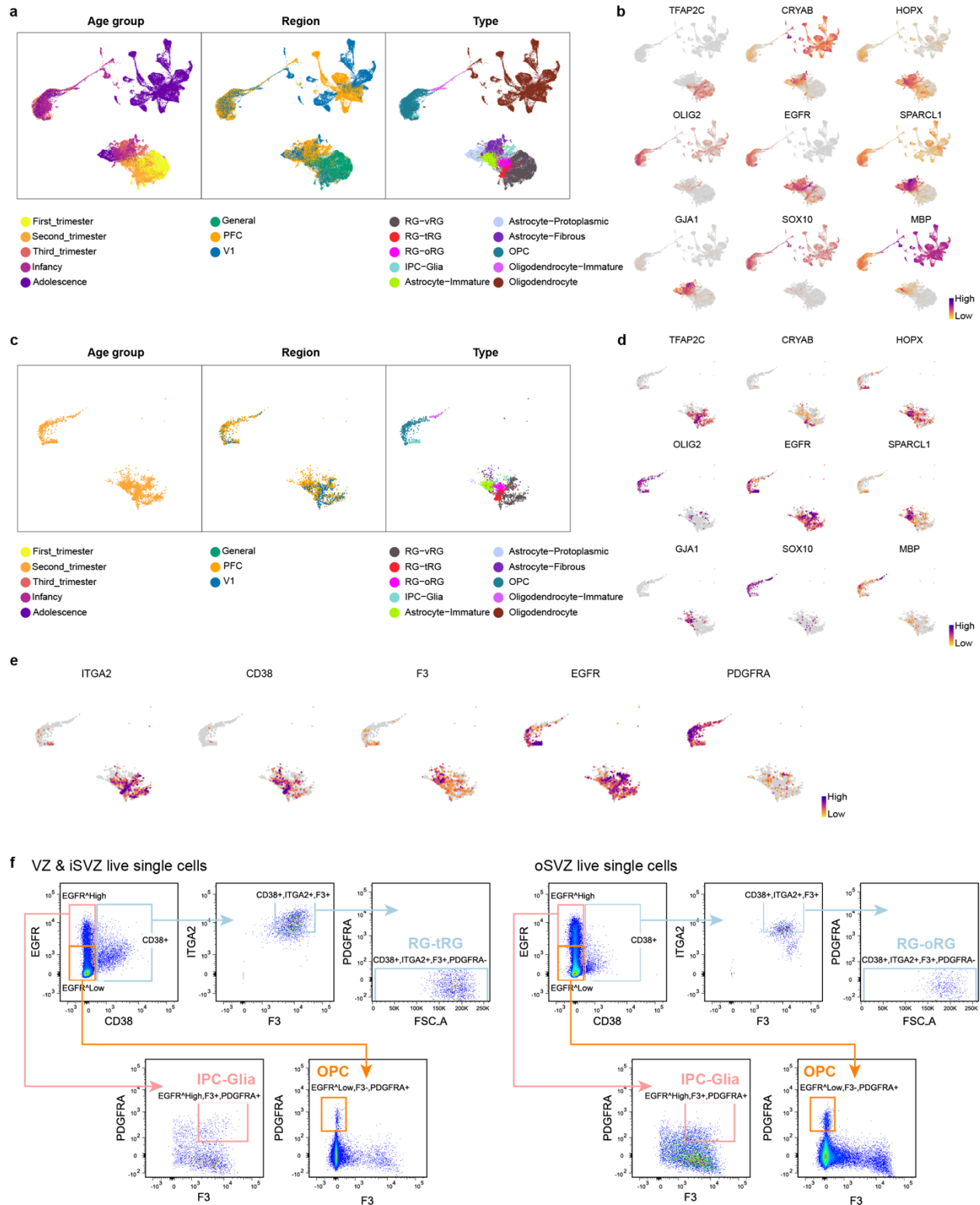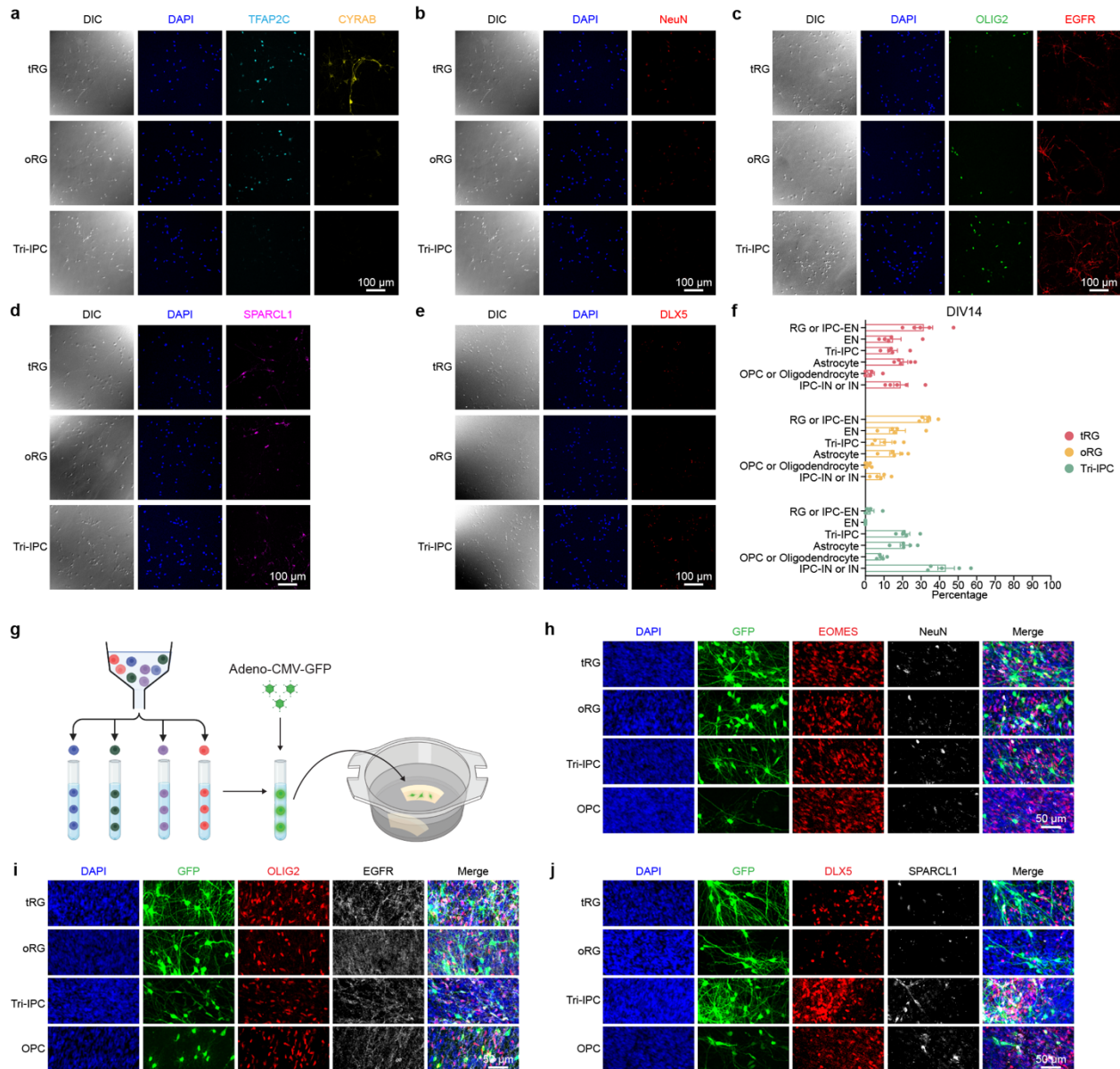
**Extended Data Fig. 10 | Markers of human glial cells and their isolation strategies. a**, UMAP plots of cells belonging to glial lineages color-coded by age groups (left), regions (middle), and types (right). **b**, UMAP plots of cells belonging to glial lineages showing the expression levels of typical marker genes of individual cell types. **c**, UMAP plots of GW20 to GW23 cells belonging

1286    to glial lineages color-coded by age groups (left), regions (middle), and types (right). **d**, UMAP
1287    plots of GW20 to GW23 cells belonging to glial lineages showing the expression levels of typical
1288    marker genes of individual cell types. **e**, UMAP plots of GW20 to GW23 cells belonging to glial
1289    lineages showing the expression levels of surface markers used for glial progenitor isolation. **f**,
1290    Schematic of the sorting strategy for glial progenitors. VZ & iSVZ, ventricular zone and inner
1291    subventricular zone; oSVZ, outer subventricular zone.

1292

1293

53
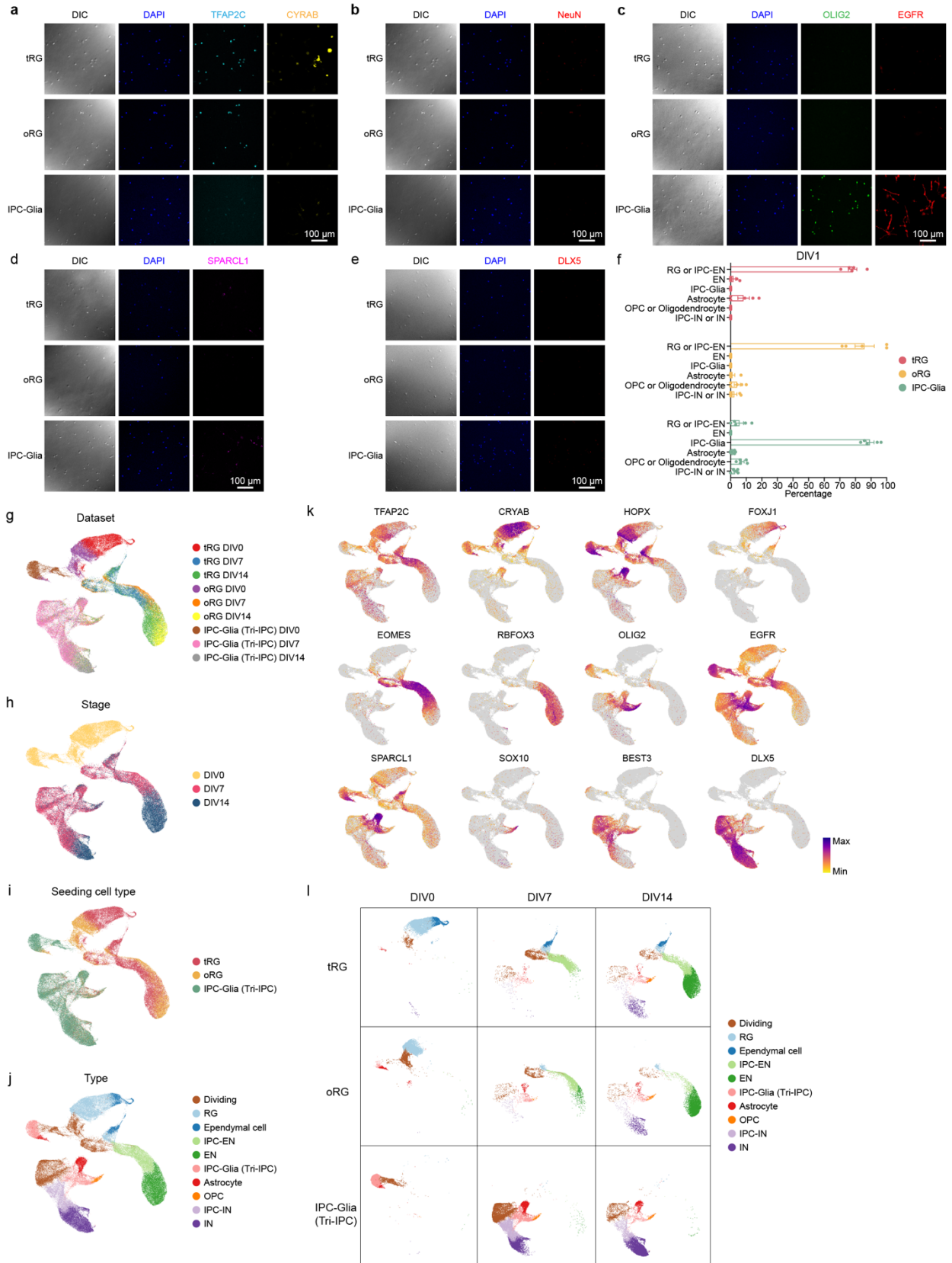
**Extended Data Fig. 11 | Characterization of human glial progenitor differentiation. a–e**, Immunostaining of isolated glial progenitors on days *in vitro* 1. **f**, Quantification of six cell types after sorting on days *in vitro* 1 (n = 5, 5, 5 samples), including RG or IPC-EN (TFAP2C$^+$), EN (NeuN$^+$), IPC-Glia (OLIG2$^+$EGFR$^+$), astrocyte (SPARCL1$^+$), OPC or oligodendrocyte (OLIG2$^+$EGFR$^-$), and IPC-IN or IN (DLX5$^+$). **g–j**, UMAP plots of isolated glial progenitors and their progenies during *in vitro* differentiation based on single-cell RNA sequencing data color-coded by datasets (**g**), stages (**h**), seeding cell types (**i**), and types (**j**). **k**, UMAP plots of isolated glial progenitors and their progenies showing the expression levels of typical marker genes of individual cell types. **i**, UMAP plots of isolated glial progenitors and their progenies separated by seeding cell types and stages.

**Extended Data Fig. 12 | Lineage potential of human glial progenitors. a–e**, Immunostaining of progenies of glial progenitors on days *in vitro* 14. **f**, Quantification of six cell types after sorting on days *in vitro* 14 (n = 5, 5, 5 samples), including RG or IPC-EN (TFAP2C$^+$), EN (NeuN$^+$), Tri-IPC (OLIG2$^+$EGFR$^+$), astrocyte (SPARCL1$^+$), OPC or oligodendrocyte (OLIG2$^+$EGFR$^-$), and IPC-IN or IN (DLX5$^+$). **g**, Schematic of the slice transplantation assay for glial progenitors. **h–j**, Immunostaining of progenies after progenitor transplantation to acute cortical slices on days *in vitro* 8.
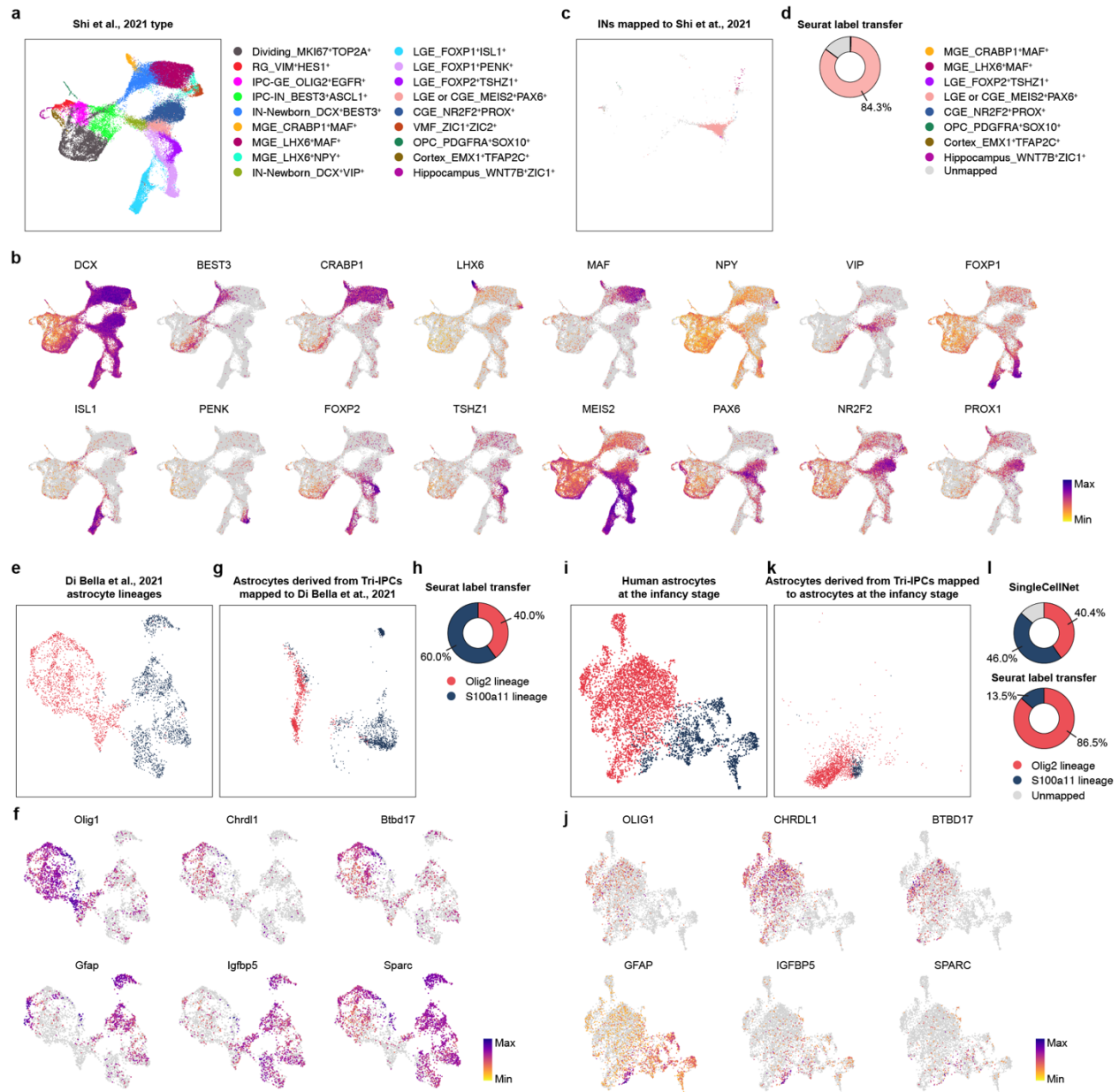
1314

**Extended Data Fig. 13 | Mapping Tri-IPC progenies to reference data. a**, UMAP plot of a reference human ganglionic eminence dataset[44]. Cells are color-coded by types. **b**, UMAP plots of human ganglionic eminence cells showing the expression levels of typical marker genes of individual cell types. **c**, UMAP plots of Tri-IPC-derived INs projected to the human ganglionic eminence dataset. Cells are color-coded by types and the legend can be found in panel d. **d**, Identities of Tri-IPC-derived INs mapped by Seurat label transfer. **e**, UMAP plot of mouse astrocytes from a reference developing mouse cortex dataset[48]. Cells are color-coded by lineages and the legend can be found in panel h. **f**, UMAP plots of the reference mouse astrocytes showing the expression levels of typical marker genes of individual astrocyte lineages. **g**, UMAP plots of Tri-IPC-derived astrocytes projected to the reference mouse astrocytes. Cells are color-coded by lineages and the legend can be found in panel h. **h**, Identities of Tri-IPC-derived astrocytes mapped by Seurat label transfer. **i**, UMAP plot of human astrocytes at the infancy stage. Cells are color-

1327    coded by lineages and the legend can be found in panel l. **j**, UMAP plots of human astrocytes

1328    showing the expression levels of typical marker genes of individual astrocyte lineages. **k**, UMAP

1329    plots of Tri-IPC-derived astrocytes projected to the reference human astrocytes. Cells are color-

1330    coded by lineages and the legend can be found in panel l. **l**, Identities of Tri-IPC-derived astrocytes

1331    predicted by SingleCellNet (top) or mapped by Seurat label transfer (bottom).

1332
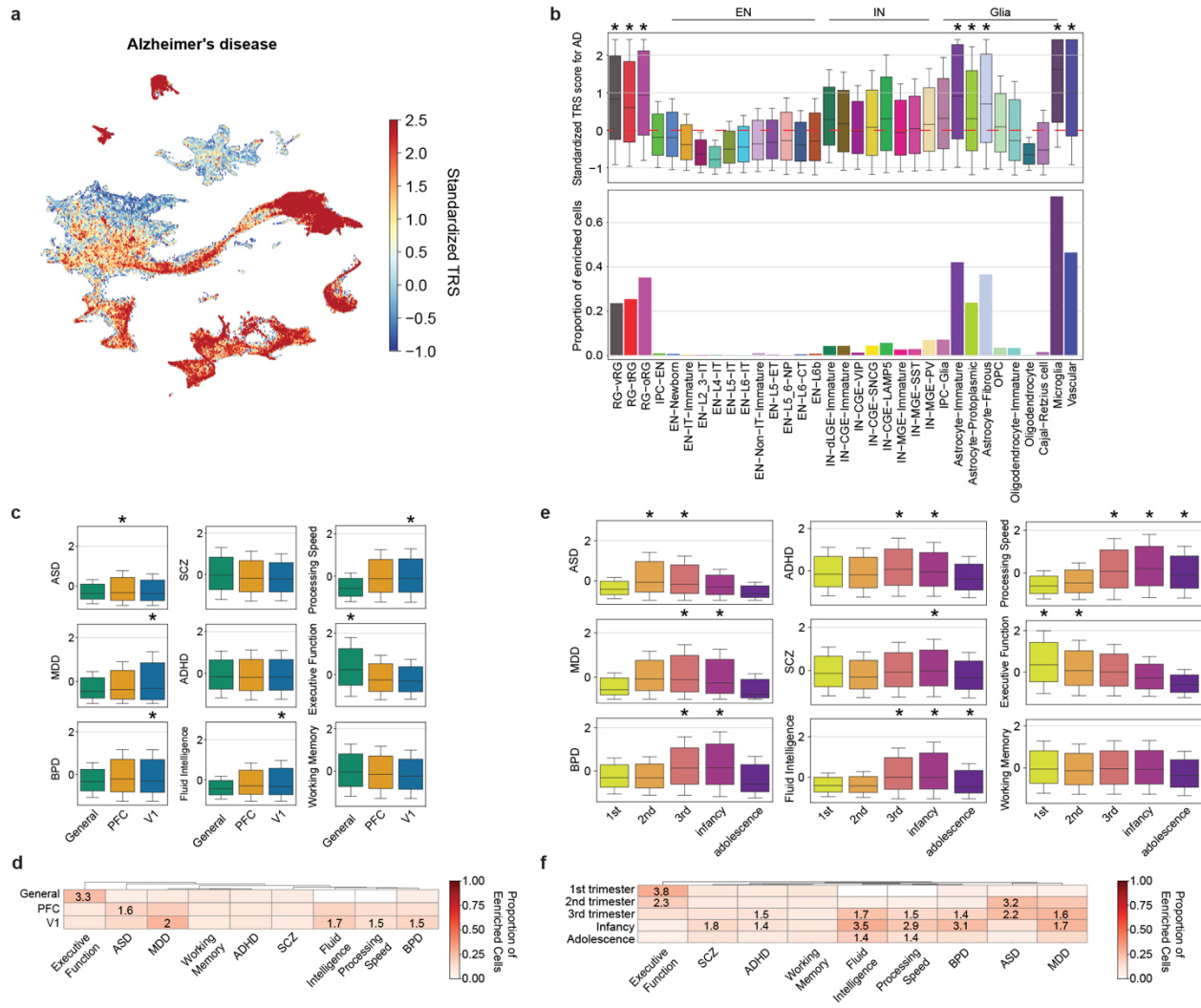
**Extended Data Fig. 14 | Neocortical cell association with human cognition and brain disorders. a**, UMAP plot showing the standardized per-cell SCAVENGE trait relevance score (TRS) for Alzheimer's disease. **b**, Top, boxplots showing the standardized SCAVENGE TRS for Alzheimer's disease across cell types. Boxplot center: median; hinges: the 25th and 75th percentiles; whiskers: standard error. Bottom, bar plots showing the proportion of the cells with enriched trait relevance for Alzheimer's disease across cell types. Hypergeometry test; *FDR < 0.01 & odds ratio > 1.4. **c**, Boxplots showing standardized SCAVENGE TRS for nine cognitive and disease traits across regions. Boxplot center: median; hinges: the 25th and 75th percentiles; whiskers: standard error. Hypergeometry test; *FDR < 0.01 & odds ratio > 1.4. **d**, Heatmap showing the proportion of the cells with enriched trait relevance across regions. Tiles with significant TRS enrichment (hypergeometric test, *FDR < 0.01 & odds ratio > 1.4) are annotated by their odd ratios. **e**, Boxplots showing standardized SCAVENGE TRS for nine cognitive and disease traits across developmental stages. Boxplot center: median; hinges: the 25th and 75th percentiles; whiskers: standard error. Hypergeometry test; *FDR < 0.01 & odds ratio > 1.4. **f**, Heatmap showing the proportion of the cells with enriched trait relevance across developmental stages. Tiles with significant TRS enrichment (hypergeometric test, *FDR < 0.01 & odds ratio > 1.4) are annotated by their odd ratios.

58